

Plateau de bure High- z Blue-Sequence Survey 2 (PHIBSS2): Search for Secondary Sources, CO Luminosity Functions in the Field, and the Evolution of Molecular Gas Density through Cosmic Time*

LAURA LENKIĆ,¹ ALBERTO D. BOLATTO,¹ NATASCHA M. FÖRSTER SCHREIBER,² LINDA J. TACCONI,² ROBERTO NERI,³ FRANCOISE COMBES,⁴ FABIAN WALTER,^{5,6} SANTIAGO GARCÍA-BURILLO,⁷ REINHARD GENZEL,^{2,8,9} AND DIETER LUTZ²

¹University of Maryland 1113 PSC Bldg., 415 College Park, MD 20742-0001

²Max-Planck-Institut für extraterrestrische Physik (MPE), Giessenbachstr., D-85748 Garching, FRG, Germany

³IRAM, 300 Rue de la Piscine, F-38406 St. Martin d'Heres, Grenoble, France

⁴Observatoire de Paris, LERMA, College de France, CNRS, PSL Univ., Sorbonne Univ. UPMC, F-75014, Paris, France

⁵Max Planck Institut für Astronomie, Königstuhl 17, 69117 Heidelberg, Germany

⁶National Radio Astronomy Observatory, Pete V. Domenici Array Science Center, P.O. Box 0, Socorro, NM 87801, USA

⁷Observatorio Astronómico Nacional-OAN, Observatorio de Madrid, Alfonso XII, 3, E-28014 Madrid, Spain

⁸Department of Physics, Le Conte Hall, University of California, Berkeley, CA 94720, USA

⁹Department of Astronomy, Campbell Hall, University of California, Berkeley, CA 94720, USA

ABSTRACT

We report on the results of a search for serendipitous sources in CO emission in 110 cubes targeting CO (2 – 1), CO (3 – 2), and CO (6 – 5) at $z \sim 1 - 2$ from the second Plateau de Bure High- z Blue-Sequence Survey (PHIBSS2). The PHIBSS2 observations were part of a 4-year legacy program at the IRAM Plateau de Bure Interferometer aimed at studying early galaxy evolution from the perspective of molecular gas reservoirs. We present a catalog of 67 candidate secondary sources from this search, with 45 out of the 110 data cubes showing sources in addition to the primary target that appear to be field detections, unrelated to the central sources. This catalog includes the redshifts, line widths, fluxes, as well as an estimation of their reliability based on their false positive probability. We perform a search in the 3D-HST/CANDELS catalogs for the secondary CO detections and tentatively find that $\sim 64\%$ of these have optical counterparts, which we use to constrain their redshifts. Finally, we use our catalog of candidate CO detections to derive the CO (2 – 1), CO (3 – 2), CO (4 – 3), CO (5 – 4), and CO (6 – 5) luminosity functions over a range of redshifts, as well as the molecular gas mass density evolution. Despite the different methodology, these results are in very good agreement with previous observational constraints derived from blind searches in deep fields. They provide an example of the type of “deep field” science that can be carried out with targeted observations.

Keywords: galaxies: high-redshift — galaxies: evolution — galaxies: ISM — galaxies: luminosity function, mass function

1. INTRODUCTION

Detailed measurements of the star formation history of the universe reveal that the process of galaxy assembly peaked about 10 billion years ago. The star formation rate (SFR) density in galaxies (i.e., total SFR in

galaxies in a comoving volume of the universe) across cosmic time is observed to gradually increase to redshifts of $z \gtrsim 2$, peak at $z \sim 1 - 2$, and then decrease from redshifts of $z \sim 1$ to the present day by almost an order of magnitude (see e.g., Madau & Dickinson 2014). The fundamental physical processes that shape this evolution, however, are still uncertain. This evolution may be driven by the availability of larger reservoirs of cold dense molecular gas (the immediate fuel for star formation) in high- z galaxies, by higher efficiencies for converting molecular gas into stars, or by a combination of both. Therefore, it is interesting to constrain the molecular gas content of galaxies over cosmic time (mea-

Corresponding author: Laura Lenkić
llenki@astro.umd.edu

* Based on observations of an IRAM Legacy Program carried out with the NOEMA, operated by the Institute for Radio Astronomy in the Millimetre Range (IRAM), which is funded by a partnership of INSU/CNRS (France), MPG (Germany), and IGN (Spain).

sured as total gas mass per co-moving volume) in order to understand the evolution of the cosmic star formation history.

Most studies of the cold molecular gas in galaxies have used CO observations, the most common molecular gas mass tracer (Bolatto et al. 2013), of galaxies that were pre-selected based on optical or near-infrared surveys. Other galaxies detected in CO at higher redshifts were initially selected from rest-frame far-infrared continuum surveys as sub-mm galaxies (Blain et al. 2002; Casey et al. 2014). These studies have shaped our understanding of the relation between molecular gas content and star formation in known populations of galaxies. Targeted CO studies find that $z \sim 2$ galaxies have much larger molecular gas reservoirs than local galaxies (Greve et al. 2005; Daddi et al. 2010; Genzel et al. 2010, 2015; Tacconi et al. 2010, 2013, 2018; Freundlich et al. 2019) and that the changes in growth history are largely driven by the cold molecular gas mass properties of galaxies. While these types of studies allow us to understand the properties of galaxy samples, they can potentially introduce unknown systematic biases through selection effects. It is therefore beneficial to complement them with blind searches for CO-emitting galaxies, which effectively are selected solely on their line flux.

Spectral scans on specific deep fields have been used to carry out blind searches targeting rotational transitions of CO over wide frequency and redshift ranges, measuring the CO luminosity function at different epochs in the history of the universe. The CO luminosity function so obtained gives a measurement of the molecular gas mass density over the range of redshifts sampled by the observations (Carilli & Walter 2013). Initial efforts that have followed this strategy are the IRAM Plateau de Bure Interferometer (PdBI) observations in the *Hubble* Deep Field North, and the Atacama Large Millimeter Array (ALMA) observations in the *Hubble* Ultra Deep Field (the ASPECS-Pilot program). These spectral scans were conducted at 3 mm and 1 mm wavelengths, covering areas of ~ 0.5 and ~ 1 arcmin² in size, respectively (see Decarli et al. 2014; Walter et al. 2016, for survey descriptions). Walter et al. (2014) and Decarli et al. (2016) present luminosity function measurements for CO (3 – 2) and higher-J transitions at $z \sim 2 - 3$, and CO (5 – 4) and higher-J transitions at $z \sim 5 - 7$. These studies provided some of the first constraints on the cosmological CO luminosity function, and the cosmic molecular gas mass density evolution, but they are limited by the small areas covered.

More recently, the COLDz project (> 300 hours of observations on the JVL A) covered a ~ 48 arcmin² area in GOODS-N and a ~ 8 arcmin² area in COSMOS in

the 30 – 38 GHz frequency range, targeting CO (1 – 0) at $z \sim 2 - 2.8$ and CO (2 – 1) at $z \sim 4.9 - 6.7$ (Pavesi et al. 2018). This survey provides constraints for the CO luminosity function at $z > 2$ (Riechers et al. 2019). The ASPECS Large Program (LP; 150 hours of observations on ALMA) covers most of the *Hubble* eXtremely Deep Field (~ 4.6 arcmin²) at 3 mm and 1.2 mm wavelengths (González-López et al. 2019). Decarli et al. (2019) use it to measure the CO luminosity function and find that the cosmic molecular gas mass density peaks at $z \sim 1.5$ and decreases by a factor of $\sim 6.5^{+1.8}_{-1.4}$ to the present day.

In this paper, we present an alternative method for measuring the CO luminosity function, and therefore the cosmic molecular gas mass density evolution, which takes advantage of independent deep observations of targeted galaxies. Specifically, we present the results from a blind CO search in the second Plateau de Bure High- z Blue-Sequence Survey (PHIBSS2) observations, the follow up to PHIBSS. PHIBSS and PHIBSS2 have been productive surveys with key results on their main objective, characterizing normal $z \sim 1 - 2$ galaxies. Among other results, PHIBSS and PHIBSS2 have yielded scaling relations for main sequence galaxies at those redshifts, depletion times and molecular fractions (Genzel et al. 2015; Tacconi et al. 2018), and characterized molecular reservoirs for $z < 1$ galaxies (Freundlich et al. 2019). However, these observations also have the potential to yield impactful “deep field” science. Since each PHIBSS2 observation targeted a galaxy selected from the 3D-HST CANDELS fields, characterization of serendipitous detections benefits from the extensive multi-wavelength coverage available in these legacy fields.

This paper is structured as follows: Section 2 summarizes the observations used, Section 3 describes the blind search algorithm, the optical counterpart search, and our statistical methods for assessing the likelihood that each candidate is real as well as the completeness of the search algorithm. Section 4 presents the results of the line search, the CO luminosity functions we derive, and the molecular gas mass density evolution constraints. Section 5 compares to previous works and Section 6 summarizes the work done. The properties of the candidate sources, their spectra, and optical counterparts are presented in the Appendices.

Throughout the paper, we assume Λ CDM cosmology with $H_0 = 70$ km s^{−1} Mpc^{−1}, $\Omega_m = 0.3$, and $\Omega_\Lambda = 0.7$, consistent with the *Wilkinson Microwave Anisotropy Probe* measurements (Komatsu et al. 2011).

2. OBSERVATIONS

2.1. The “Plateau de Bure High- z Blue-Sequence Survey” (PHIBSS)

The PHIBSS2 survey is an IRAM Plateau de Bure Interferometer (PdbI; [Guilloteau et al. 1992](#)) 4-year legacy program aimed at studying early galaxy evolution from the perspective of molecular gas reservoirs, while exploiting the capabilities of the Northern Extended Millimeter Array (NOEMA; [Schuster 2014](#)) as they came online. Observations of $^{12}\text{CO}(2-1)$, $^{12}\text{CO}(3-2)$, and $^{12}\text{CO}(6-5)$ transitions took place between October 2013 and June 2017. Observation times per target range from 0.6 to 30.3 hours, with a total of $\sim 1,100$ hours of 6-antenna equivalent on source integration time, and were mostly taken in C configuration to ensure that the galaxies are not spatially resolved (see [Freundlich et al. 2019](#), for more details on the data reduction process). Given the integration times and configurations, the synthesized beams range from $1''$ to $5''$. At the redshifts targeted by PHIBSS, the typical scales are $6-8.5$ kpc per arcsec.

The survey consists of 110 individual observations of main sequence galaxies, exploring the $\text{CO}(2-1)$, $\text{CO}(3-2)$, and $\text{CO}(6-5)$ line emission, covering a total area of ~ 130 arcmin 2 and sampling a total co-moving volume of ~ 200000 Mpc 3 (see Table 4.3).

2.2. Ancillary Data

We use the 3D-HST/CANDELS survey catalogs ([Brammer et al. 2012](#); [Skelton et al. 2014](#); [Momcheva et al. 2016](#)) for the COSMOS, GOODS-N, and EGS/AEGIS fields to search for optical counterparts. We present cutouts from the HST Advanced Camera for Surveys (ACS) for filter F814W for each field (where possible) corresponding to the PHIBSS2 observations in Appendix A (see §4.1.1). For targets lying outside the area covered by the HST ACS optical or WFC3 near-IR mosaics, we show cutouts of Spitzer IRAC 3.6 μm images.

3. METHODS

3.1. Line Search

The goal of the line search is to systematically select candidate sources from noisy data, and assess their significance in terms of their corresponding signal-to-noise ratio (SNR). For our sample of observations, we expect sources to be unresolved and to mostly have FWHM in the range of $\sim 50-500$ km s $^{-1}$, and at most ~ 1000 km s $^{-1}$. [Rubin et al. \(1985\)](#) shows massive galaxies have maximum rotation velocities that span from $\sim 100-400$ km s $^{-1}$, while small irregular galaxies have minimum rotation speeds of $\sim 50-100$ km s $^{-1}$, and [Carilli & Walter \(2013\)](#) show that hyper-starburst quasar hosts and sub-

millimeter galaxies can have line widths up to ~ 1000 km s $^{-1}$.

Our line search method is a 1D matched filter technique where we select a Hanning kernel as our template. We Hanning-smooth and decimate each observation five times, where each iteration of the smoothing increases the width of a channel by a factor of two while removing one every two channels (that is, decimating the highly correlated channels). This creates cubes with velocity resolutions spanning from ~ 7 to ~ 1000 km s $^{-1}$, depending on the observation (the original data cubes have channel widths ranging from 7 to 88 km s $^{-1}$). The purpose of this matching is to maximize the signal-to-noise for signals of a given line-width. Hence our choice of smoothing allows us to attempt to match the velocity resolution of the data cube with that of the potential sources in the data. Each data cube generates five additional smoothed cubes corresponding to the different velocity resolution templates.

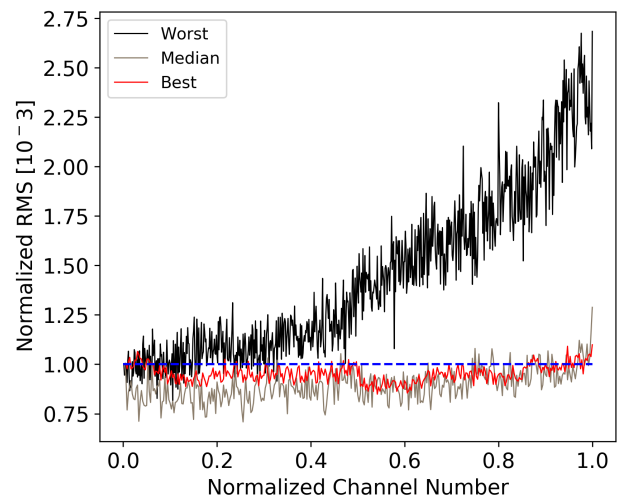


Figure 1. RMS as a function of channel number (both normalized to unity), showing a typical best case scenario (red line) where the RMS is approximately flat across all channels, a typical worst case scenario (black line) where the RMS varies quite significantly across the channels, and a median case (beige line). This illustrates the need to properly model the RMS variations across the passband in order to correctly estimate the SNR of every pixel. We do this by modeling the RMS variations as a function of frequency with a seventh order polynomial for each data cube.

For each of these cubes (original and smoothed), we compute a significance (SNR) map by taking the peak value at each pixel along the spectral axis and dividing it by the RMS (taken to be the standard deviation) of the spectral channel. The RMS as a function of channel number (frequency) is usually fairly flat, but occasion-

ally it can vary quite substantially across the passband. We illustrate this in Figure 1, where we show three examples of how the noise varies across channels in three different data cubes. For the purpose of comparison, we normalize the X and Y axes to unity. We plot a typical best case scenario in red, a typical worst case scenario in black, and a median example in beige, while the dashed blue line serves as a reference point for a straight horizontal line. It is therefore important to properly account for this when calculating the SNR in order to not over or underestimate the SNR of a given pixel. To characterize this variation, we fit the distribution of the channel RMS as a function of channel number for each data cube with a polynomial, in order to have a smooth representation of the large-scale noise variation to properly calculate SNR. We then divide each peak pixel by the corresponding channel RMS from our fit. The order of the polynomial chosen to obtain our smooth representation of the noise is not particularly important, and a value of seven was found to produce very reasonable results.

In order to obtain the distribution of the noise, we repeat this process for the negative peaks, that is dividing the largest negative peak at each pixel by the channel RMS, thus creating SNR maps of “negative emission”. Positive emission corresponds to real astrophysical sources as well as noise peaks, while “negative emission” corresponds only to noise. The most significant negative peak therefore provides an estimate of what is the boundary between likely noise and likely signal. From these SNR maps, we build a list of candidate sources by selecting pixels with a positive SNR value that is greater than the absolute value of the largest negative peak SNR. We save a list of all pixels that satisfy this condition, sort it by decreasing SNR, and filter out all pixels that lie within one beam of the highest SNR pixels to arrive at a list of independent possible sources. We perform this search and filtering on all smoothed cubes and then combine the lists into one list, where we filter out candidate sources that satisfy our detection threshold in multiple cubes for a given field (original and/or smoothed cubes), but with lower SNR. This leaves us with a final list of candidate sources for each field in our sample, where the position of each source corresponds to the position of the most significant pixel for the velocity smoothing parameter that provides the highest SNR. Figure 2 shows an example SNR map for one of our fields (eg016; see Table A) at a velocity resolution of 352 km s^{-1} , with the black contour showing the threshold of the most significant negative peak in that cube, our chosen boundary between “likely noise”

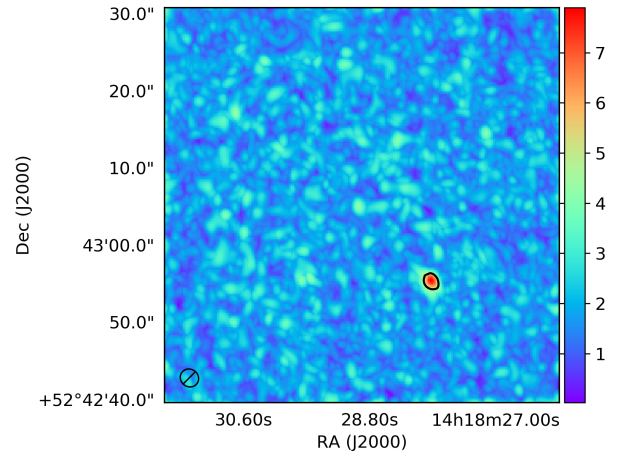


Figure 2. Hanning-smoothed SNR map for the eg016 data cube, at a velocity resolution of 352 km s^{-1} . The black contour corresponds to the SNR level of the largest negative peak in this cube, which is our detection threshold and in this case corresponds to a SNR of 4.93. A single source appears in this map with SNR above the detection threshold we impose (see eg016-1 in Table A for physical properties). The central targeted source in the eg016 data cube has a SNR of 3.1 (see Table 3 in [Freundlich et al. 2019](#)), which is below our detection threshold and is therefore not visible in this SNR map.

and “likely signal”. In what follows we estimate the probability of this candidate source being real.

3.1.1. False Positives

The purpose of the false positive analysis is to assign to each candidate source a probability of it being a real astrophysical source, which we will call reliability (also called fidelity or purity). To address this question, we use the statistics of the negative emission, which consists of only noise, to determine the likelihood that noise could produce a SNR as large as that of each candidate source.

In order to estimate this we would ideally consider the statistics of independent points in the map. In our significance maps, in principle all pixels within one beam of a strong emission pixel will be correlated. To remove from our distribution of peak SNR values pixels that are correlated, we perform a “cleaning” of the map. We do that by taking the most significant value in a given map, subtracting a beam-like Gaussian from that pixel position, and then repeating the process until no values above $3 \times$ the RMS level of the map remain, leaving us with a list of independent “sources” in terms of SNR. As a comparison, we do the same thing with the SNR map distribution of positive peaks.

The distributions of independent positive and negative peaks in a given map overlap very well, and are

well approximated by a Gaussian with an exponential tail toward high significance (Figure 3). However, the tail of the distribution is the region that we are interested in characterizing because this is where the candidate sources we detect lie. To achieve this goal, we begin by normalizing the distribution of independent positive and negative peaks so that their integrals equal unity. We then treat the normalized independent negative distribution as our probability density function, which we fit with an exponentially modified Gaussian distribution of the form:

$$h(x) = \frac{\lambda}{2} e^{\frac{\lambda}{2}(2\mu + \lambda\sigma^2 - 2x)} \text{erfc}\left(\frac{\mu + \lambda\sigma^2 - x}{\sqrt{2}\sigma}\right) \quad (1)$$

where x corresponds to the peak SNR values of the inverted cube, μ and σ are the mean and standard deviation of the Gaussian, λ is the rate of the exponential, and erfc is the complementary error function which is equal to $1 - \text{erf}(x)$. This function describes a Gaussian distribution with a positive skew due to an exponential component. An example of this fit is shown in Figure 3, where the orange histogram corresponds to the SNR distribution of the negative emission, the blue histogram is the SNR distribution of the positive emission, and the black line is the exponentially modified Gaussian; the bottom panel shows the residuals. Figure 3 corresponds to the data cube eg016 (Table A), where one candidate source is identified as possible emission through the line search procedure described above.

To estimate the probability that the observed significance could be produced by noise fluctuations, we use the cumulative distribution of the exponentially modified Gaussian distribution, which has the form:

$$H(x) = \Phi(u, 0, \sigma) - e^{-u+v^2/2+\log(\Phi(u, v^2, v))} \quad (2)$$

where $u = \lambda(x - \mu)$ and $v = \lambda\sigma$, and $\Phi(x, \mu, \sigma)$ is the cumulative distribution function of a Gaussian distribution with mean μ and standard deviation σ .

For a given candidate source, the probability that a random fluctuation produces a source with SNR greater than or equal to that of the candidate source, (i.e., falls in the range $x \in [\text{SNR}_{\text{src}}, \infty)$), is:

$$P(x > \text{SNR}_{\text{src}}) = 1 - H(\text{SNR}_{\text{src}}). \quad (3)$$

For each candidate source, this gives an estimate of the probability that a given independent measurement (a beam) in the map could have a peak SNR greater than or equal to that of the candidate source itself. To assess the significance of these values, we compare them to the number of independent beams sampled by each

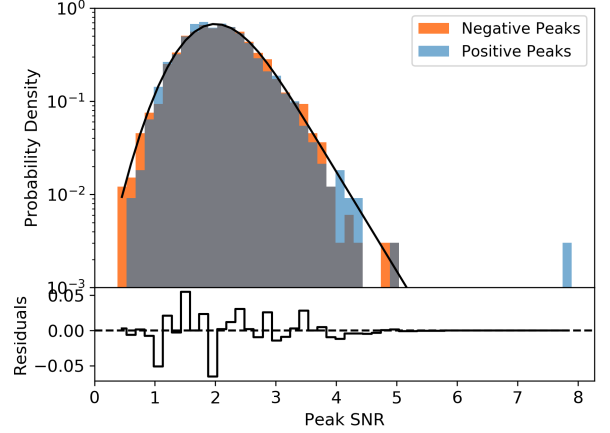


Figure 3. The top panel shows the distribution of positive (blue) and negative (orange) peak SNRs per beam of the eg016 data cube, at a velocity resolution of 352 km s^{-1} (the gray histogram is the overlap of the blue and orange histograms). The black line is the exponentially modified Gaussian fit to the negative peaks distribution. We see one object with positive peak SNR much greater than the largest negative peak SNR (in absolute values); this corresponds to the candidate sources. The bottom panel shows the residuals from fitting with an exponentially modified Gaussian function, which we find represents that data reasonably well.

SNR map. We do this by taking the inverse of the false positive probability we calculate from equation 3 as a measure of how many random measurements it would take to observe the given candidate source SNR value once (i.e., one in every N number of measurements will have an SNR equal to or greater than what is observed for the candidate source given only noise; we call this N_{expected}). Then the ratio of N_{expected} to the number of independent beams sampled (N_{beams}) by each SNR map is the total number of measurements with a given SNR we would expect to make due to noise only. For very strong candidate sources this number is very small, and for weaker sources it becomes larger and can become on the order of unity. The reliability parameter (R) we assign to each source is one minus this ratio:

$$R = 1 - \frac{N_{\text{expected}}}{N_{\text{beams}}} \quad (4)$$

Our reliability measurements range from $0.01 - 1$ (i.e., $1 - 100\%$ reliability), and we include in our sample candidate sources with $R > 5\%$ since this is the threshold adopted by [Riechers et al. \(2019\)](#). We show these values in Table A. Note that we do not attempt to further filter our list of candidate sources by choosing a higher reliability cutoff. There is a strong correlation between integrated flux and reliability, where fainter sources with lower SNR naturally tend to show lower R (see §4.2, Fig-

ure 7). The derivation of the luminosity function (§4.3) properly takes into account the statistics by weighting by reliability, and artificially inserting a high reliability cutoff would cause us to preferentially remove the contribution from fainter sources. Note also that computation of R for the central sources, all known to be real, shows a large spread driven by SNR. So it is clear that real sources can have low reliability when they are faint in relation to the noise of the observation.

3.1.2. Completeness

To assess the completeness of our search algorithm, we perform an analysis of the chance of detecting sources we artificially inject into each data cube. The purpose of this analysis is to relate the fraction of recovered simulated sources to the line flux. Since we do not expect resolved sources in the PHIBSS2 data, we do not account for varying sources sizes.

To simulate sources, we assume a Gaussian line profile along the spectral axis, and generate sources with five free parameters: the spatial position, the peak flux density of the line, its velocity width as FWHM, and the velocity of the peak by drawing random numbers from a uniform distribution. The x and y coordinates are limited to integers between 1 and 256, since the cubes are 256×256 pixels in size. The peak flux density of each artificial source ranges between the maximum value in the data and 1% of the maximum. The FWHM is limited to $150 - 300 \text{ km s}^{-1}$.

We then assume that each source will be “beam-like”, so we take the flux density at each velocity channel that the source appears in to be the peak of a two-dimensional Gaussian which has the same position angle and size as the synthesized beam for each data cube. We generate 2500 artificial sources for each data cube in this way, add them to the data cube 5 sources at a time to avoid crowding, run the search algorithm, and check the fraction of sources recovered. Figure 4 plots the fraction of recovered artificial sources as a function of integrated flux (blue circles), for the eg016 data cube. The recovered fraction is fit with a Gaussian cumulative distribution function (solid blue line). The vertical dashed black lines correspond to the integrated flux of the candidate sources for this data cube. We can see that the recovery fraction decreases with decreasing integrated flux, which is known for each simulated source. We correct for completeness on a source-by-source basis using the cumulative Gaussian distribution fit for each data cube. Given the integrated flux of each candidate source, x , the corresponding completion correction is

$$C(x) = \frac{1}{2} \left[1 + \operatorname{erf} \left(\frac{x - \mu}{\sigma\sqrt{2}} \right) \right], \quad (5)$$

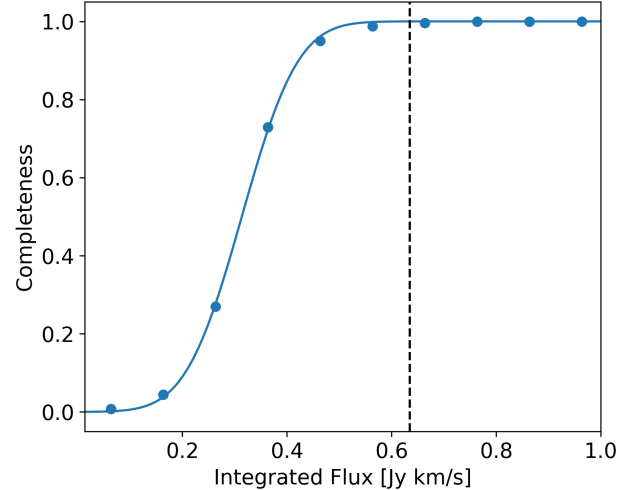


Figure 4. The fractions of recovered sources to artificial sources injected as a function of integrated flux for the eg016 field, from our analysis of 2500 simulated sources shown as blue dots. The blue line is a fit to this distribution using a cumulative Gaussian distribution. The vertical dashed lines correspond to the integrated flux of the candidate source. As we would expect, the recovery of sources decreases with decreasing integrated flux indicating that fainter sources are harder to detect than brighter ones. This analysis allows us to correct our CO luminosity functions for the incompleteness of our search algorithm, particularly at the faint end where this becomes a larger effect (see §4.3).

where μ and σ are the mean and standard deviation derived from our Gaussian cumulative distribution function fit for a given cube.

4. RESULTS OF LINE SEARCH

4.1. Line Properties

We extract the spectrum of each candidate source at the position of the peak SNR pixel, given that the sources in PHIBSS2 are unresolved, in each field at all velocity resolutions, and apply a primary beam correction. These spectra are fit with a Gaussian profile using Python’s `scipy.optimize.curve_fit`. Spectra of all candidate sources with reliability over 60% detected in the 110 data cubes analyzed are presented in the right panels of Figure 14 for sources in the COSMOS fields, Figure 15 for sources in GOODS-N, and Figure 16 for sources in EGS/AEGIS in Appendix A.

The redshift of each candidate source is calculated from the central frequency of the line, assuming that the emission detected corresponds to a CO transition from CO (1–0) to CO (6–5). CO emission represents usually the brightest line in galaxy spectra at wavelengths between 400 and 2600 μm . Rotational transitions of CO are spaced by intervals of 115.27 GHz, so with a sin-

gle transition by itself it is impossible to determine the redshift of the source. The optical counterpart search discussed in the next section allows us to, in some cases, determine which CO transitions a candidate source may correspond to, and in other cases, to constrain the range of possible CO transitions.

The flux and full-width-half-maximum of each candidate source are calculated from the best fit standard deviation and amplitude of the Gaussian profile fit. These results are presented in Table A in Appendix A.

4.1.1. Optical Counterparts

The purpose of identifying counterparts (CPs) for the candidate sources is to constrain their likely redshift and CO transition, as well as properties like their stellar masses and SFRs. We search for all optical sources in the 3D-HST/CANDELS catalogs (Brammer et al. 2012; Skelton et al. 2014; Momcheva et al. 2016) that lie within one beam FWHM radius of the peak SNR position of each candidate source we identify in PHIBSS2, while leaving the redshifts unconstrained. The objects in these catalogs have a distribution of redshifts determined from HST and ground-based spectral energy distribution (SED) fitting using the EAZY code (Brammer et al. 2008). To match the redshifts, we then consider all transitions from CO (1 – 0) to CO (6 – 5) and check which, if any, CO transitions are plausible given the posterior likelihood distributions of the redshift determination from the SED fitting. In several cases the redshifts of the optical counterparts are poorly constrained by the SED fitting, allowing a range of possible CO transitions. When grism or spectroscopic redshifts are available, we compare our redshifts to those because they are much better constrained than the photometric redshifts. For the purpose of constructing the CO luminosity functions, we assign a “redshift probability” to each source based on the posterior likelihood distribution. We also assign an “association probability” for candidate CO sources where multiple optical counterpart candidates lie within the synthesized beam of the CO data cube (which changes from cube to cube). This “association probability” is proportional to the inverse square projected angular distance between the candidate CO source and candidate optical counterpart (following the idea that the number of chance associations will increase as the area searched increases), normalized to unity.

From this spatial matching, and CO transition/redshift association, we find that $\sim 64\%$ (43 out of 67) of source candidates in our catalog have at least a tentative optical counterpart. The lack of an optical counterpart in the 3D-HST/CANDELS catalog (rest frame optical/UV

counterparts) could imply that the candidate source is spurious, or it could be physically caused by heavy extinction associated with the molecular gas (in which case there may be infrared counterparts). Whitaker et al. (2017) investigate the relation between dust obscured star formation and stellar mass as a function of redshift ($z = 0 - 2.5$). They find that for $\log(M/M_{\odot}) > 10.5$, more than 90% of star formation is obscured by dust at all redshifts, and that at $z > 1$, there is a tail of heavily obscured low-mass star-forming galaxies. This highlights the importance of infrared data, and future work may involve carrying out a systematic infrared counterpart search beyond existing catalogs (e.g., *Spitzer* IRAC 3.6 and 4.5 μm).

The results of our search are presented in the middle panel of the figures in Appendix A. These are for the most part HST ACS F814W images where the red crosses mark the positions of the candidate optical counterparts for candidate CO sources where one could be tentatively identified. For candidate sources where no ACS optical and/or WFC3 near-IR data was available, we present *Spitzer* IRAC 3.6 μm images. In the left panel, the redshifts reported correspond to the CO transition that most closely matches the “best” redshift reported in the 3D-HST/CANDELS catalogs. In the computation of the CO luminosity functions, we however use the range of possible CO transitions/redshifts allowed by the potential counterparts to derive CO luminosities, weighted by their respective probabilities (see §4.3 for details). Finally, these results are also summarized in Table 3 where we give the right ascension, declination, and “best” redshift reported in the 3D-HST/CANDELS catalogs of each optical counterpart. We also provide the CO based redshifts for the range of possible CO transitions as determined from the EAZY SED fitting posterior likelihood distributions. Finally, we provide the angular separation between the candidate source and potential optical counterpart, with a probability of association in cases where more than one possible counterpart exists within the synthesized beam.

In Figure 5 we compare the integrated flux, line width, and reliability of candidate sources with potential optical counterparts (dark blue, right-hatched histogram), and those without (lighter blue, left-hatched histogram). In all three cases, both populations of candidate sources span the same parameter space. Both populations contain many fainter objects and fewer bright objects, so while some of those may be spurious detections, the reliability distribution shows that there are several high-reliability objects with no optical counterpart identified. In terms of line width, both populations span essentially the same range of line widths probed.

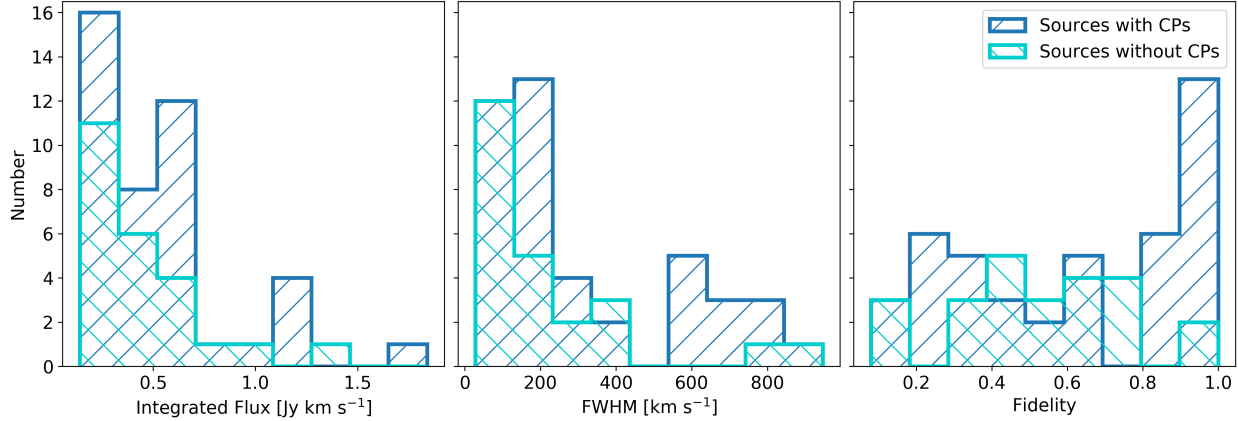


Figure 5. Comparing the properties of the candidate sources with optical counterparts (dark blue, right-hatched histogram) to those without (cyan, left-hatched histogram). *Left:* comparing the integrated flux, *Middle:* comparing the line width (FWHM), *Right:* comparing the reliability. The K-S test results indicate that the distributions are similar in terms of all three properties.

To quantify this we perform the Kolmogorov-Smirnov test and find a K-S statistic of $D_{n,m} = 0.21, 0.25$, and 0.36 for the integrated flux, FWHM, and reliability distributions respectively (where n and m are the lengths of the two samples). The K-S statistic is the maximum distance between the cumulative distributions of the two compared populations, so a small enough K-S statistic indicates that the hypothesis that two samples are drawn from the same distribution cannot be rejected. Specifically, the two samples can be said to come from different distributions at a confidence level α if

$$D_{n,m} > c(\alpha) \sqrt{\frac{n+m}{nm}} \quad (6)$$

where

$$c(\alpha) = \sqrt{-\frac{1}{2} \ln \alpha}. \quad (7)$$

From the K-S statistics for these three distributions, we find that the hypothesis that both samples are drawn from the same distribution can be rejected at the 74.4%, 86.1%, and 98.1% confidence level for the integrated flux, FWHM, and reliability respectively. These confidence levels are usually not considered significant enough to reject the hypothesis. We conclude from this that the candidate sources without counterparts are similar to the candidate sources with counterparts, although they tend to be fainter and consequently less reliable.

For candidate sources where we identify possible counterparts (and hence for which we have a redshift z), we compare the molecular gas mass from the CO luminosity to the molecular gas inferred from the potential counter-

part SFR, using the depletion time scale scaling relation of Tacconi et al. (2018):

$$\log(t_{dep}) = A_t + B_t \log(1+z) + C_t \log(\delta MS) \quad (8)$$

where $A_t = 0.09$, $B_t = -0.62$, $C_t = -0.44$ (for details see Tacconi et al. 2018), and δMS is the offset from the main sequence of a source. Using the redshift, and main sequence offset of the potential counterpart, we calculate their depletion timescales and then infer the molecular gas mass based on their SFR (since $t_{dep} = M_{gas}/\text{SFR}$).

We plot this comparison in Figure 6, omitting candidate sources with multiple possible counterparts identified within one synthesized beam and sources where the product of the CO source reliability (R) times the counterpart probability of association (P_a) is less than 50%, as we consider these sources and/or counterparts not highly reliable. The size of the data points is scaled according to the product of the reliability and the probability of association (higher $R \times P_a$ correspond to larger symbols), and colored according to redshift. The black solid line is the one-to-one relation and the black stars are primary PHIBSS2 targets plotted as a comparison. These all lie on the one-to-one line, except for one target, which has a large offset from the main sequence of star formation ($\log \delta MS = +2.41$, corresponding to a target over the main sequence) and therefore a very short depletion timescale. In contrast, the majority of potential counterparts lie systematically below the one-to-one relation, which would imply molecular gas reservoirs larger than would be inferred from the measured star formation.

The SFRs reported in the 3D-HST/CANDELS catalog for these objects are derived from SED modeling. We have used the catalog by Momcheva et al. (2016), but

with SFR values recomputed according to the Herschel-calibrated ladder of indicators in Wuyts et al. (2011) (see also Tacconi et al. 2018, and references therein). The SEDs for all objects contain optical to $8\ \mu\text{m}$ photometry, and some objects have photometry at longer wavelengths. At the redshifts of these objects, $8\ \mu\text{m}$ corresponds to rest-frame wavelengths of $\lambda \sim 1.5 - 4\ \mu\text{m}$. For six data points the photometry also includes $24\ \mu\text{m}$ to $160\ \mu\text{m}$ measurements. These are indicated by vertical dashed lines, which join the SFR obtained from fitting the $\lambda \leq 8\ \mu\text{m}$ photometry to the SFR computed including the longer wavelengths (which corresponds to the square symbols in Figure 6). When the SED modeling includes only the shorter wavelengths, it results in SFRs one to two orders of magnitude lower than is estimated when longer wavelength data are included. The agreement between molecular masses estimated from the optical counterpart star formation activity, and those directly measured in the PHIBSS2 observations, is very good when the SFR estimate includes $\lambda \geq 24\ \mu\text{m}$ information.

Our identification process naturally selects objects that are bright in CO, and indeed they all have very large molecular masses as inferred from their flux. Therefore they are likely dust-rich, and their star formation activity is highly extinguished. It appears likely that the dust-obscured component of star formation is not properly accounted for when the longest rest-frame wavelength included in the SED is $\lambda \sim 1.5 - 4\ \mu\text{m}$. We believe this is the main cause for the majority of the large discrepancies between the two estimates of molecular gas mass. It is also possible, particularly for sources with low reliability or probability of association, that some of them are not real or that some counterparts are misidentified. The agreement between the CO luminosity function we derive from these data (§4.3) and other measurements in the literature, however, suggests that this is not the case for the majority of our objects.

4.2. Comparing Serendipitous Detections to Central Sources

The goal of PHIBSS2 is to study galaxy evolution from the perspective of molecular gas reservoirs. Surveys such as PHIBSS2 that target specific galaxies selected based on their stellar mass, SFR, and availability of ancillary data have complex selection functions. The blind search we have performed here, and our catalog of serendipitous detections provide a sample of objects that are mostly free of selection biases, other than the selection function imposed by the redshift ranges surveyed in any given observation and the flux which makes brighter objects

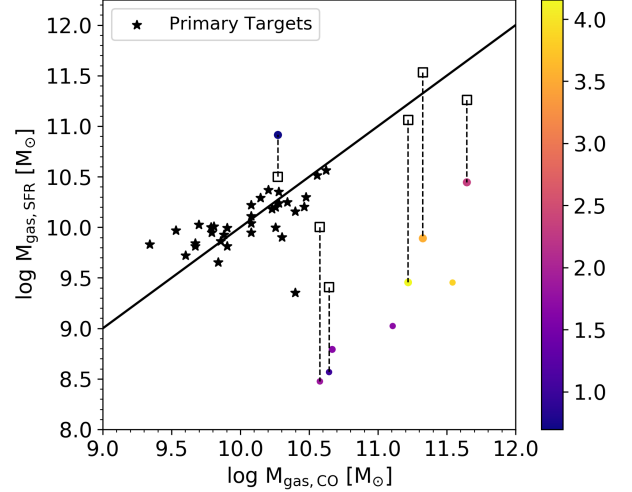


Figure 6. Comparison of the molecular gas mass measured from the candidate source CO luminosities to the molecular gas mass inferred from the potential optical counterpart SFR and the depletion timescale scaling relation of Tacconi et al. (2018). The size of the colored points is scaled according to the product of reliability and association probability of the detection, and they are colored according to redshift. The diagonal black solid line is the one-to-one relation. All colored symbols correspond to SFR measurements from SED modeling of optical to $8\ \mu\text{m}$ photometry; the black square symbols show the effect of including longer wavelength photometry (24 or $160\ \mu\text{m}$) on the SFR calculation for the sources where that is available.

easier to detect. We can therefore compare these two samples to get an idea of their respective biases.

In the left panel of Figure 7, we compare the integrated fluxes of all 67 candidate sources to those of the central sources targeted by PHIBSS2. In the right panel of Figure 7, we compare the molecular gas masses of the candidate sources with tentative optical counterpart identifications to that of the central sources. The central sources are plotted as the blue hatched histogram and the candidate sources are separated into histograms corresponding to likelihood levels: the hatched magenta histogram corresponds to sources with reliabilities between 5 and 50%, the orange filled histogram corresponds to sources with reliabilities between 50 and 90%, and the yellow histogram corresponds to sources with reliabilities greater than 90%.

We see in the flux comparison that the sample of central sources and the sample of secondary candidate detections seem to generally probe objects with similar properties. Performing a K-S test, we find that $D_{n,m} = 0.13, 0.19, 0.34$, which results in rejecting at the 54.0%, 73.3%, and 95.4% confidence level the hypothesis that the candidate source distributions come from the same

distribution of central sources for the 5–50%, 50–90%, and > 90% reliability ranges respectively. These are not strong rejections, suggesting that regardless of the reliability, the candidate secondary sources have properties that are very similar to those of the central targeted sources. In terms of molecular mass, our higher reliability candidate sources seem to correspond to slightly more massive objects not well represented in the original PHIBSS2 sample, selected to represent the main sequence at the redshifts of interest. In both panels we see that the fainter/less massive candidate sources tend to have lower reliabilities than the brighter/more massive objects. This is not surprising, since these candidates will have lower SNRs.

We observe across our sample of candidate detections and tentative optical counterpart identifications that some candidate sources lie at redshifts similar to that of the central target source. This raises the question of whether constructing a CO luminosity function from data targeted at particular objects introduces biases due to possible clustering of sources around the targeted object. To evaluate whether this is the case, we compare in Figure 8 the difference between the frequency of each candidate source and the frequency of the central source in each data cube ($\Delta\nu$; left panel). We also show the difference between the redshift of the central source and candidate source, for candidates with identified counterparts (Δz ; right panel). In both cases we also compare the distribution of $\Delta\nu$ and Δz when weighting the data by reliability, probability of association, and redshift probability.

The left panel of Figure 8 shows in both the unweighted and weighted cases that the candidate sources are approximately uniformly distributed in $\Delta\nu$ with a slight decrease for $\Delta\nu \gtrsim 1$ and a bit of a central bump for completely unweighted sources. However, the data cubes do not all cover the same frequency range and therefore the chance of a source to show at a particular $\Delta\nu$ has to be weighted accordingly. To account for this, we normalize the reliability weighted histogram by the number of data cubes that span the different possible $\Delta\nu$ ranges. This is shown in the gray histogram, where we see that the recovered distribution is very consistent with a uniform distribution across the spectral range. This shows that our secondary detections are uniformly distributed in $\Delta\nu$, and therefore there is no signature of a bias introduced by clustering around the targeted central sources. In physical terms, $\Delta\nu = 1$ GHz for a source at $z \sim 1.5$ in a $\lambda \simeq 3$ mm observation represents a physical velocity difference of over $3,000 \text{ km s}^{-1}$, larger than the central velocity dispersion of a massive galaxy cluster like Coma ($\sigma_V \sim 1200 \text{ km s}^{-1}$, Kent & Gunn 1982).

Therefore we would expect a relatively narrow peak in the corrected histogram if most sources were physically related to the central source, independent of our ability to identify counterparts.

The right panel of Figure 8 shows the distribution in Δz for only those candidate sources for which we find tentative optical counterparts. The unweighted case shows a wide peak in the distribution of objects at $z \pm 1$ from the central sources. When weighting by reliability, probability of association, and redshift probability this peak is significantly smoothed but still present. The existence of a broad peak is to be expected: most of our observations target the 2–1 and 3–2 CO transitions at $z \sim 1–2$, and the most likely bright transitions for field objects will be 2–1 to 4–3, which would place them in the $\Delta z \sim \pm 1$ range for most observations. Note also that if this were an indication of true physical clustering we would expect the peak to be much narrower, $\Delta z \lesssim \pm 0.1$.

4.3. CO Luminosity Functions

We construct the CO luminosity functions using equation 9:

$$\Phi(\log L_i) = \frac{1}{V} \sum_{j=1}^{N_i} \frac{R_j}{C_j} P_{a,j} P_{z,j}. \quad (9)$$

Here N_i is the number of galaxies that fall within the luminosity bin i defined by $\log L_i - 0.25$ and $\log L_i + 0.25$ ($\log L_i - 0.5$ and $\log L_i + 0.5$ for cases where we only have a small number of sources), V is the total volume of the Universe that is sampled by a given transition across all of our data cubes, F_j is the reliability of the j^{th} line and C_j is its completeness, $P_{a,j}$ is the probability that the candidate source is associated with a particular optical counterpart, and $P_{z,j}$ is the probability that a given candidate optical counterpart corresponds to a particular CO transition (and hence redshift). Each CO line is down-weighted by its likelihood probability calculated in §3, probability of association, and redshift probability, and then up-scaled by its completeness fraction. The CO luminosities are calculated from equation 3 of Solomon et al. (1997):

$$L'_{CO} = 3.25 \times 10^7 \frac{S_{CO} \Delta V D_L^2}{\nu_{obs}^2 (1+z)^3} \quad [\text{K km s}^{-1} \text{ pc}^2] \quad (10)$$

where $S_{CO} \Delta V$ is the integrated flux density in units of Jansky kilometers per second, D_L is the luminosity distance of the source in megaparsecs, ν_{obs} is the observed frequency of the line in GHz, and z is its redshift. The volume of the Universe that is sampled by a given

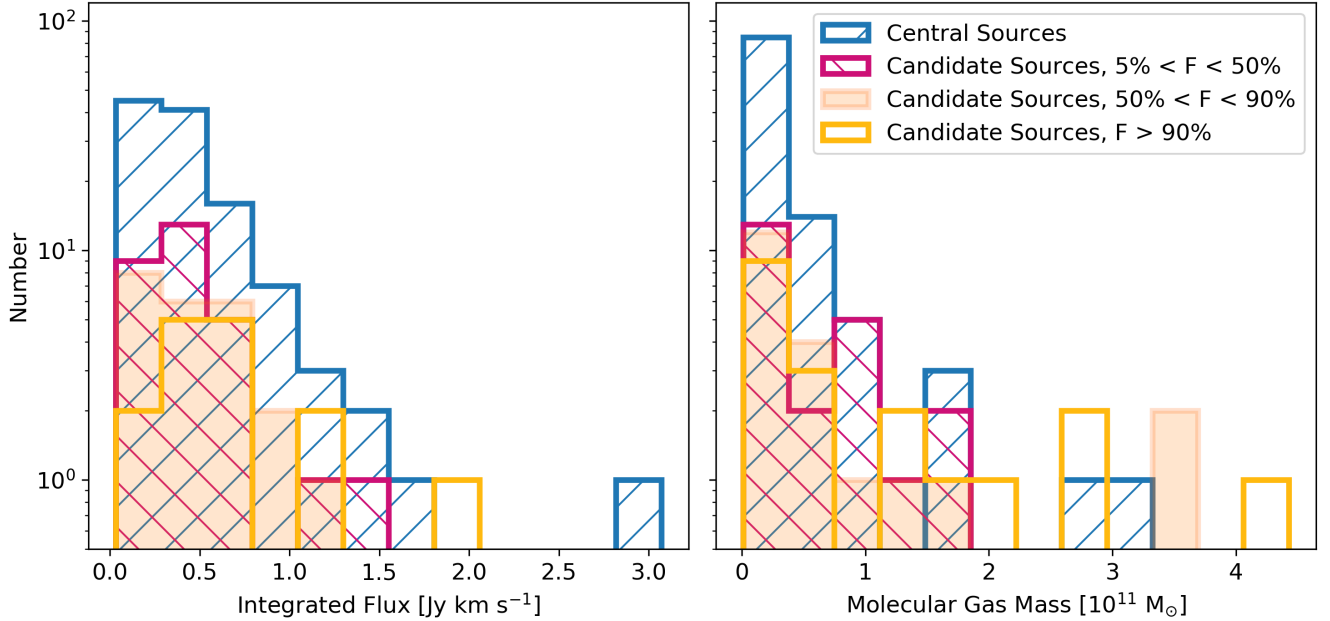


Figure 7. *Left:* Comparison of the integrated flux measurements of the central galaxies that were specifically targeted by PHIBSS2 (blue hatched histograms) to the additional serendipitous CO detections. The candidate sources are divided according to their likelihood parameter. The candidate sources generally seem to follow a similar distribution of fluxes as the targeted central sources. A K-S test reveals that at the 48.2%, 94%, and 96.6% confidence level, the candidate source distributions do not come from the same distribution as the central sources (for the 5 – 50%, 50 – 90%, and > 90% reliability ranges). These weak rejections suggest that the samples are representative of the same parent population of objects. *Right:* The same as the left panel, but now comparing the molecular gas masses. The highest reliability objects tend to have the higher molecular gas masses.

PHIBSS2 data cube is calculated as a three-dimensional slab of space defined by the field-of-view of the given observation, and frequency range that is observable by the instrument, for each CO transition we consider in our counterpart search. These values are summarized in Table 4.3.

We exclude from our CO luminosity functions all central sources since these were targeted objects and are therefore not the result of our blind search. We also exclude objects with no optical counterpart identification, because we have no information on their corresponding redshift or CO transition.

4.3.1. PHIBSS2 CO Luminosity Functions

Figure 9 plots the PHIBSS2 CO luminosity function for a range of CO transitions and median redshifts in gray shaded boxes. Our results are plotted as a moving average, by displacing each luminosity bin by 0.1 dex and recalculating the CO luminosity function according to equation 9. In each panel, we give the number of candidate sources used to derive the given CO luminosity function and their median redshift. We are able to constrain CO (2 – 1) at $\langle z \rangle \sim 0.7$ and 1.2, CO (3 – 2)

at $\langle z \rangle \sim 1.5$ and 2.2, CO (4 – 3) at $\langle z \rangle \sim 1.9$, 2.2 and 3.3, CO (5 – 4) at $\langle z \rangle \sim 3.4$ and 4.4, and CO (6 – 5) at $\langle z \rangle \sim 3.7$. We compare each of these to existing theoretical predictions from Popping et al. (2019)¹, Popping et al. (2016), Vallini et al. (2016), and Lagos et al. (2012) and where possible, to existing observational constraints. To be able to consistently compare with the work of Walter et al. (2014) and Decarli et al. (2016, 2019), we calculate our uncertainties on the CO luminosity function in the same way. Thus the error bars along the y-axis correspond to Poissonian errors on N_i , the number of sources within a luminosity bin i , at the 1σ level according to Tables 1 and 2 of Gehrels (1986), while the “error bars” along the x-axis simply reflect the width of the luminosity bin.

We fit our observed CO luminosity functions with a Schechter function (Schechter 1976) in the logarithmic

¹ We convert the molecular hydrogen mass functions to CO luminosity functions assuming an $\alpha_{\text{CO}} = 3.6 \text{ M}_{\odot} (\text{K km s}^{-1} \text{ pc}^2)^{-1}$ and temperature ratios of $r_{J1} = 0.76 \pm 0.09$, 0.42 ± 0.07 for $J = 2, 3$ respectively (Daddi et al. 2015).

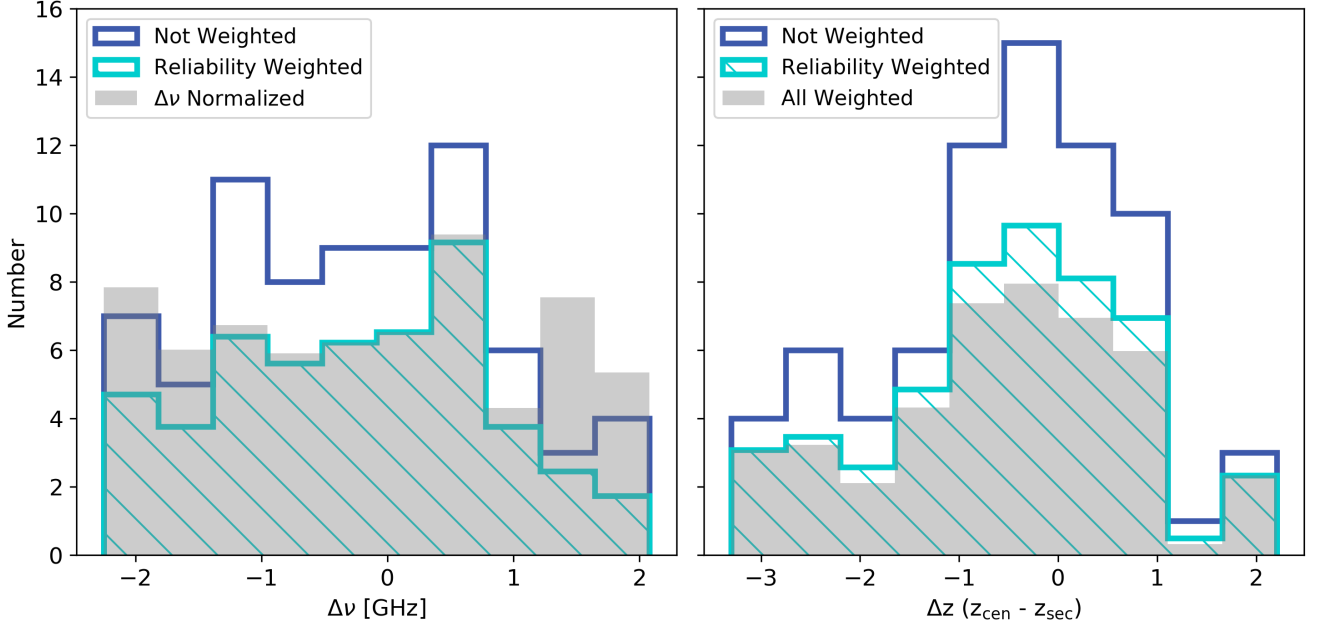


Figure 8. *Left:* Difference between the central frequency of each candidate source and the reference frequency of the observation, $\Delta\nu$. The dark blue empty histogram is unweighted by reliability, while the cyan left hatched histogram is weighted by reliability. The grey shaded histogram is the reliability weighted distribution normalized to the number of data cubes that cover a large enough frequency range to reach a given $\Delta\nu$ value. For randomly distributed objects, we would expect a flat distribution and this is what we observe. *Right:* Difference between the redshift of the central source and candidate source (only for cases where a tentative optical counterpart is identified), Δz . The dark blue empty histogram is the unweighted data, the cyan hatched histogram is weighted by reliability, and the grey shaded histogram is weighted by reliability, the probability of association, and the redshift probability. There is a tendency here for objects to cluster around $\Delta z \pm 1$, however this is too large of a redshift separation to form physical associations. We conclude the candidate sources we detect are not biased by clustering around the central source.

form used by Riechers et al. (2019) and Decarli et al. (2019):

$$\log \Phi(L') = \log \Phi^* + \alpha \log \left(\frac{L'}{L'^*} \right) - \frac{1}{\ln 10} \frac{L'}{L'^*} + \log(\ln(10)) \quad (11)$$

where Φ^* is the scale number of galaxies per unit volume, L'^* is the scale line luminosity and the parameter that sets the “knee” of the luminosity function, and α is the slope of the faint end.

To obtain estimates of the allowed range of Schechter parameters, we fit the characteristic parameters described above to our CO (2–1) at $\langle z \rangle = 0.68$ luminosity function due to the small numbers of sources in all other cases. To account for the uncertainties of each luminosity bin, we draw points from normal distributions centered in each luminosity bin, with standard deviation corresponding to the size of the luminosity bin. We fit a Schechter function to that set of points while assuming unconstrained priors on the characteristic Schechter parameters. We then repeat the process with a new set of randomly drawn points from each luminosity bin and do

this until enough points have been drawn to determine the posterior likelihood distributions of each Schechter parameter.

We show the results of this fitting in Figure 10, where we also include the posterior likelihood distribution of each parameter along with the 5th, 50th, and 95th percentiles. In Figure 11, we show the density of Schechter function fits to each sample of points drawn from the data. This Figure shows that the uncertainties are dominated by the faint end, below the “knee” of the luminosity functions. However, the three parameters L'_{CO}^* , Φ_{CO}^* , α are fairly reliably constrained by the data. We summarize the constraints on the Schechter model parameters for each fit in Table 11, including the 5th and 95th percentiles.

4.4. Molecular Gas Mass Density Evolution

To derive constraints on the evolution of co-moving molecular gas mass we need to convert our high-J CO luminosities to CO (1–0) luminosities. We assume Rayleigh-Jeans brightness temperature ratios of $r_{\text{J1}} = 0.76 \pm 0.09$, 0.42 ± 0.07 , 0.31 ± 0.06 , and 0.23 ± 0.04 for

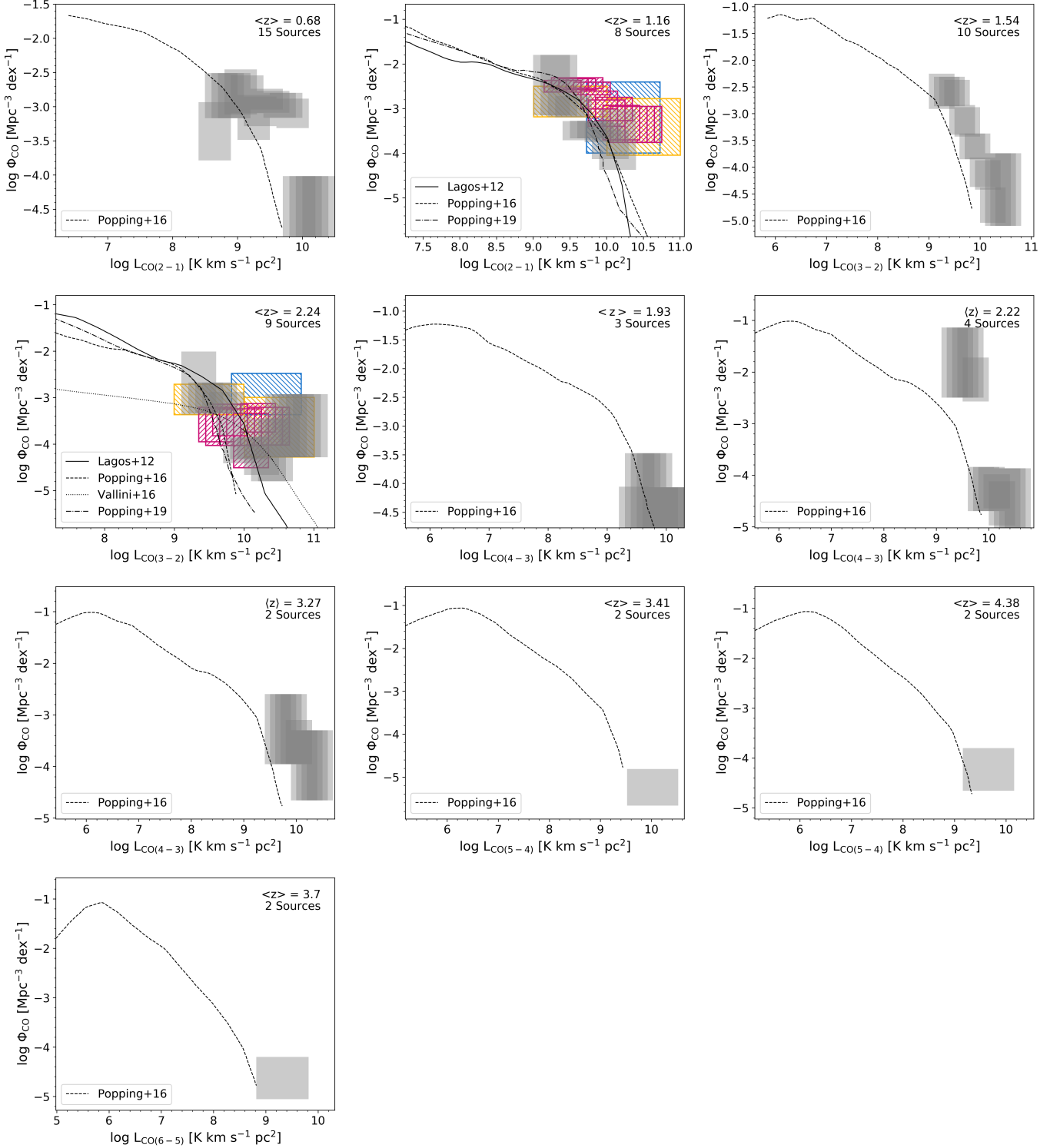
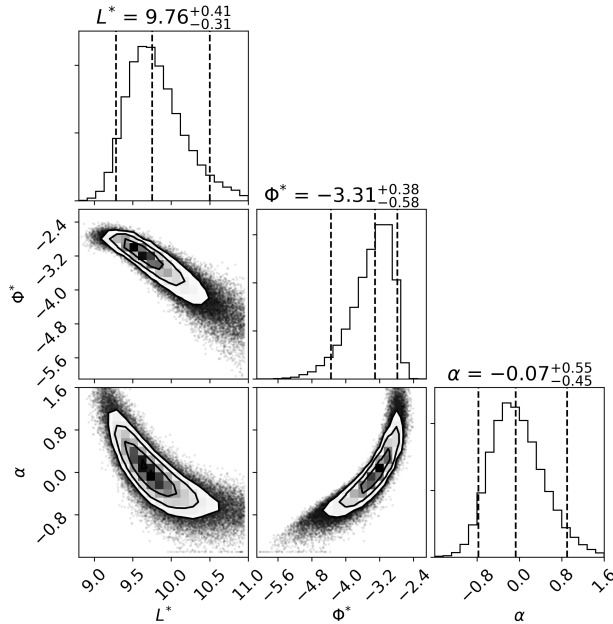
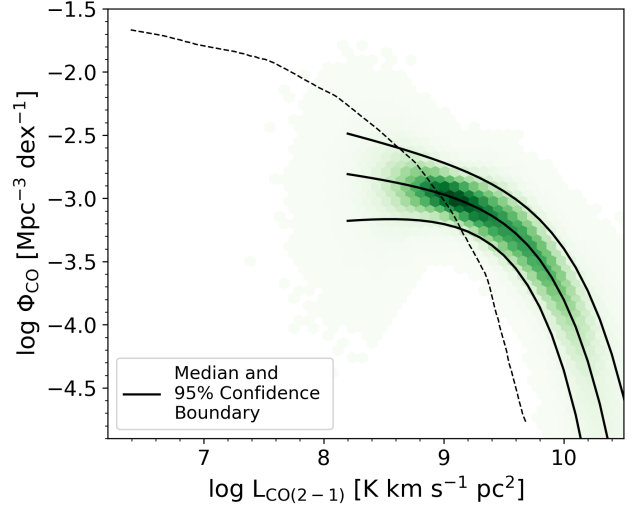


Figure 9. The PHIBSS2 CO luminosity functions observed here (shaded gray boxes, with sizes corresponding to 1σ uncertainties), compared to the PdBI HDF-N work (blue left-hatched boxes; [Walter et al. 2014](#)), the ASPECS pilot work (yellow left-hatched boxes; [Decarli et al. 2016](#)), the ASPECS LP work (magenta right-hatched boxes; [Decarli et al. 2019](#)), the predicted CO luminosity function of [Vallini et al. \(2016\)](#) based on the *Herschel* IR luminosity function, and the theoretical predictions of [Lagos et al. \(2012\)](#) and [Popping et al. \(2016\)](#). Our derived CO luminosity functions are consistent with constraints from previous work, but are in tension with the semi-analytic model predictions, particularly at the higher-J CO transitions where we observe larger number densities at higher CO luminosities than is predicted by these models.

Table 1. Comoving Volume Sampled by each CO Transition

Transition	ν_{rest}	z_{min}	z_{max}	Volume	CV
	[GHz]			[Mpc ³]	[%]
PHIBSS2					
CO (2 – 1)	230.538	0.017	1.562	13541	18.2
CO (3 – 2)	345.538	0.492	2.843	31954	15.9
CO (4 – 3)	461.041	0.989	4.124	44503	14.9
CO (5 – 4)	576.268	1.486	5.405	52387	13.3
CO (6 – 5)	691.473	1.983	6.685	57360	15.6
COLDz COSMOS					
CO (1 – 0)	115.271	1.953	2.723	20189	36.9
CO (2 – 1)	230.538	4.906	6.445	30398	37.8
COLDz GOODS-N					
CO (1 – 0)	115.271	2.032	2.847	131042	25.5
CO (2 – 1)	230.538	5.064	6.695	193286	25.6
ASPECS LP					
CO (1 – 0)	115.271	0.003	0.369	338	59.4
CO (2 – 1)	230.538	1.006	1.738	8198	36.9
CO (3 – 2)	345.538	2.008	3.107	14931	35.0
CO (4 – 3)	461.041	3.011	4.475	18242	35.2

**Figure 10.** Corner plot of the Schechter model parameters posterior distribution from fitting the CO (2 – 1) luminosity function. The parameters are reasonably well constrained by the data.**Figure 11.** Density of Schechter fits for the CO (2 – 1) $z \sim 0.7$ luminosity function. The black lines correspond to the median points and the boundary where 95% of the fits lie. For reference, the Popping et al. (2016) prediction is plotted at the dashed black line. We see from this that the “knee” of the CO luminosity function is well constrained by the data, while there is more uncertainty in constraining the slope of the faint end.**Table 2.** Schechter Function Fit Parameter Constraints from PHIBSS2

Line	Redshift	$\log L'_{\text{CO}}^*$	$\log \Phi_{\text{CO}}^*$	α
CO (2 – 1)	0.33 – 0.99	$9.76^{+0.41}_{-0.31}$	$-3.31^{+0.38}_{-0.58}$	$-0.07^{+0.55}_{-0.45}$

$J = 2, 3, 4$, and 5 respectively (Daddi et al. 2015). We then convert these CO (1 – 0) luminosities to molecular gas masses, using an α_{CO} value of $3.6 \text{ M}_{\odot} (\text{K km s}^{-1} \text{ pc}^2)^{-1}$ for the sake of consistency with previous work using

$$M_{\text{H}_2} = \alpha_{\text{CO}} L'_{\text{CO}(1-0)}. \quad (12)$$

The PHIBSS project has consistently used a 20% larger value of α_{CO} (Tacconi et al. 2018). Carleton et al. (2017) investigate the dependence of the conversion factor α_{CO} on total mass surface density for $z > 1.7$ in the PHIBSS sample of galaxies and find that 92 – 100% of α_{CO} measurements are similar to the Milky Way value of $4.36 \text{ M}_{\odot} (\text{K km s}^{-1} \text{ pc}^2)^{-1}$ adopted by PHIBSS. Here we use a value of 3.6 to compare consistently to other results in the literature who have adopted this value (Riechers et al. 2019; Decarli et al. 2019). Adopting a different constant value of α_{CO} will result in a straightforward linear scaling of our M_{H_2} and $\rho(\text{H}_2)$ measurements.

As in [Walter et al. \(2014\)](#), [Decarli et al. \(2016\)](#), [Riechers et al. \(2019\)](#), and [Decarli et al. \(2019\)](#), we do not extrapolate to the undetected faint end of the luminosity functions and only use actual candidate sources. We should note that this conversion from high-J CO transitions to molecular mass is increasingly uncertain as J increases: this is unavoidable as the excitation requirements become increasingly stringent, and so a diminishing fraction of the gas emits brightly in these transitions. The only way around this constraint is to directly observe the $J=1-0$ or $2-1$ transitions at high redshift, but that requires more powerful facilities than those in existence (such as the ngVLA, [Decarli et al. 2018](#)). Our results are shown as black boxes in Figure 12, where each box corresponds to the combination of candidate sources observed at any transition in the given redshift range.

5. DISCUSSION

5.1. Comparison to Previous Blind CO Surveys

5.1.1. Luminosity Functions

The CO $(2-1)$ at $\langle z \rangle \sim 1.2$ and the CO $(3-2)$ at $\langle z \rangle \sim 2.3$ were previously constrained by [Walter et al. \(2014\)](#), [Decarli et al. \(2016\)](#), and [Decarli et al. \(2019\)](#). The observational constraints from [Walter et al. \(2014\)](#) are the result of a blind CO survey in part of the *Hubble* Deep Field North. [Decarli et al. \(2016\)](#) observed a ~ 1 arcmin region of the *Hubble* Ultra Deep Field (UDF) with ALMA (the ASPECS pilot program), while [Decarli et al. \(2019\)](#) derive their constraints from the ASPECS Large Program. The redshift ranges for which we derive constraints from CO $(2-1)$ and CO $(3-2)$ are very similar to these previous works, so we directly compare our measurements to them. We see from Figure 9 that our results correspond to approximately the same luminosity bins as [Decarli et al. \(2016\)](#), and are in agreement with their results. [Decarli et al. \(2016\)](#) report an excess of CO-bright galaxies in the UDF with respect to theoretical predictions, and our results confirm this for the galaxies we observe in the 3D-HST/CANDELS fields sampled by our PHIBSS2 data. This implies that galaxies in this redshift bin are more gas-rich than is currently predicted by theoretical models.

[Riechers et al. \(2019\)](#) derive the CO $(1-0)$ luminosity function for a median redshift of $z = 2.4$ in the COLDz program. Our CO $(3-2)$ luminosity function is derived for a median redshift of $z \sim 2.3$. We consider this difference in redshift to be negligible and therefore compare to the COLDz measurements without any modifications. To compare these results then, it is only necessary to assume a line ratio between these two transitions. To

convert our CO $(3-2)$ luminosities to CO $(1-0)$ we use $r_{31} = 0.42 \pm 0.07$ from [Daddi et al. \(2015\)](#).

We show the comparison between our derivation and that of the COLDz results of [Riechers et al. \(2019\)](#) in Figure 13. Overall we find that our measurements are consistent with those of [Riechers et al. \(2019\)](#) within the uncertainties, although there is a hint that our results may point to higher number densities than those measured in COLDz. This could be due to cosmic variance (CV), or it could also be evidence that higher-J observations or surveys tend to preferentially select higher gas excitation galaxies. This would then mean that our temperature ratio is too low. [Bolatto et al. \(2015\)](#) find for two CO $(3-2)$ bright $z \sim 2.2-2.3$ galaxies r_{31} ratios of order unity, while samples of nearby galaxies, luminous infrared galaxies, and ultra luminous infrared galaxies show mean values of $r_{31} \sim 0.66$. We convert our CO $(3-2)$ luminosities to CO $(1-0)$ using this higher temperature ratio and show the result in Figure 13 (dashed black boxes). The change in assumed excitation produces a moderate shift toward lower luminosities, which brings the data into somewhat better agreement but does not completely eliminate the tension between both sets of measurement.

5.1.2. Molecular Gas Mass Density Evolution

In Figure 12, we compare our results to all previous observational constraints: those from [Walter et al. \(2014\)](#), the ASPECS pilot work of [Decarli et al. \(2016\)](#), the COLDz measurements of [Riechers et al. \(2019\)](#), and the ASPECS LP measurements of [Decarli et al. \(2019\)](#). Within the uncertainties, our results are consistent with all previous observational constraints. Between redshifts of $z \sim 2-3$, our result is most consistent with the measurement of [Walter et al. \(2014\)](#) and the ASPECS pilot, and hints at maybe a higher molecular gas mass density than that obtained by COLDz. From redshifts of $z \sim 3-5$, our measurements are consistent with the ASPECS pilot measurements, and hints at a lower molecular gas mass density than derived in the ASPECS-LP. Given the present state of the art in the uncertainties it is unclear if these discrepancies are real, but their magnitude is easily explained by cosmic variance.

5.2. Cosmic Variance

To address the question of cosmic variance, we use the results of [Driver & Robotham \(2010\)](#) to quantify the cosmic variance of the PHIBSS2 data. The authors repeatedly extract galaxy counts in cells of fixed size at random locations in the Sloan Digital Sky Survey (SDSS) Data Release 7. They explore the variance of the SDSS data in square cells from 1 to 2048 square degrees and in rectangular cells with aspect ratios ranging from 1:1 to

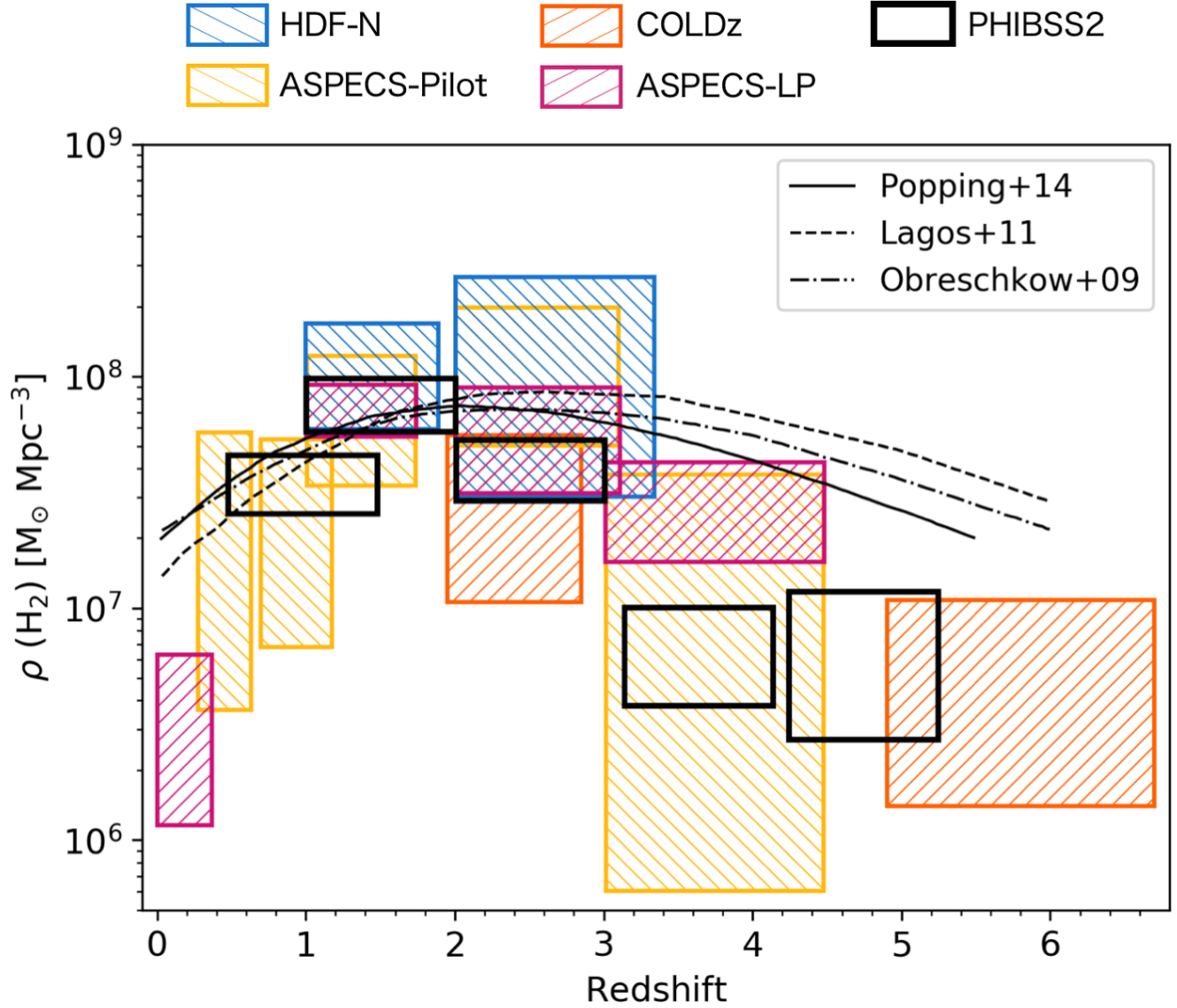


Figure 12. The evolution of the molecular gas mass density with redshift, where the black boxes represent the constraints from the PHIBSS2 data. Orange right hatched boxes correspond to the constraints derived from the VLA COLDz measurements of [Riechers et al. \(2019\)](#), purple right hatched boxes correspond to the constraints of ASPECS LP measurements of [Decarli et al. \(2019\)](#), yellow left hatched boxes correspond to the work of [Decarli et al. \(2016\)](#), and the blue left hatched boxes correspond to the constraints from the work of [Walter et al. \(2014\)](#). The dashed lines correspond to model predictions for the evolution of the molecular gas mass density, as derived by [Obreschkow et al. \(2009\)](#), [Lagos et al. \(2011\)](#), and [Popping et al. \(2014a\)](#), [Popping et al. \(2014b\)](#). The constraints derived from serendipitous detections of CO in the PHIBSS2 fields are consistent with those of previous blind surveys.

1:128. They find that cosmic variance depends on total survey volume, the survey aspect ratio, and whether the survey area is contiguous or composed on independent lines of sight, with cosmic variance decreasing for higher aspect ratios and non-contiguous survey areas (which essentially help sample a larger range of environments). [Driver & Robotham \(2010\)](#) provide a general equation that can be used at any redshift to estimate the cosmic

variance of a survey (eq. 4 in [Driver & Robotham 2010](#)):

$$\zeta_{\text{Cos.Var.}}(\%) = (1.00 - 0.03\sqrt{(A/B)-}) \times [219.7 - 52.4 \log_{10}(AB \times 291.0) + 3.21[\log_{10}(AB \times 291.0)]^2] / \sqrt{NC/291.0} \quad (13)$$

where A and B are the transverse lengths at the median redshift, C is the radial depth all expressed in

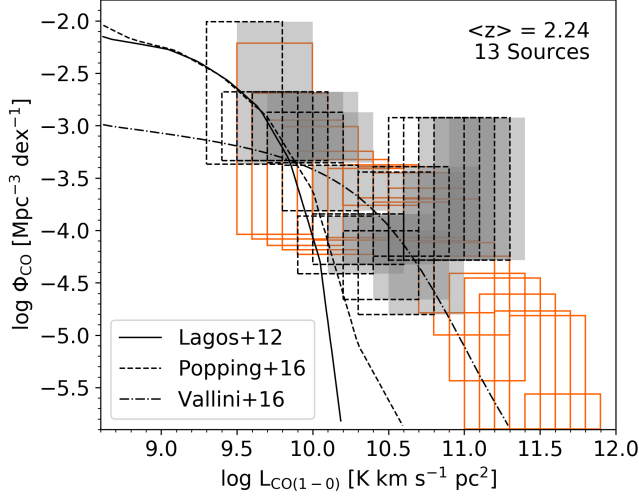


Figure 13. The comparison of our CO (3 – 2) luminosity function, converted to CO (1 – 0) assuming a brightness temperature ratio of $r_{31} = 0.42$ (gray boxes) to the results of Riechers et al. (2019) (orange boxes). Within the uncertainties, our measurements are consistent with those of Riechers et al. (2019). There is a hint at maybe higher number densities, particular at lower CO luminosities. As an additional comparison, we convert out CO (3 – 2) luminosities with a $r_{31} = 0.66$ (Bolatto et al. 2015, black dashed boxes). This shifts our measurements to lower CO luminosities bringing them into better agreement with Riechers et al. (2019). We plot the predictions of Lagos et al. (2012); Vallini et al. (2016); Popping et al. (2016) as a reference.

units of $h_{0.7}^{-1}$ Mpc, and N is the number of independent sightlines. This empirical expression for estimating the cosmic variance is implemented as a function in the R library `celestial`, as `cosvarsph`. We input into `cosvarsph` the RA, Dec, and redshift limits that correspond to those values of the PHIBSS2 data cube with the median volume (since not all data cubes have the same size), and finally take N to be the total number of data cubes. With this estimate, we derive cosmic variances in the range $\sim 13\% - 18\%$; these values are summarized in the last column of Table 4.3.

For comparison, we perform a crude estimate of the cosmic variance in the COLDz survey. The COLDz survey covers an area of 8.9 arcmin^2 at 31 GHz and 7.0 arcmin^2 at 39 GHz for COSMOS and an area of 50.9 arcmin^2 at 30 GHz and 46.4 arcmin^2 at 38 GHz. Using the average area and the redshift limits reported in their Figure 1 for both the CO (1 – 0) and CO (2 – 1) transitions as inputs into `cosvararea`, we estimate a cosmic variance of $\sim 34\%$ and $\sim 24\%$ for COSMOS and GOODS-N respectively. Performing the same estimate for the ASPECS-LP using the redshift limits from Table 1 of Decarli et al. (2019), we find that the cosmic

variance in the range $\sim 59\%$ to $\sim 35\%$ for CO (1 – 0) to CO (4 – 3). These estimates are for a square survey area with aspect ratio 1:1, which is only approximate for either the COLDz or the ASPECS-LP surveys, and are therefore likely upper limits on their cosmic variance. However, this still shows that cosmic variance may be less of an issue in surveys that are composed of multiple independent lines of sight rather than one contiguous area.

6. CONCLUSIONS

We present a catalog of 67 candidate secondary sources observed in 110 observations of PHIBSS2, where the primary target is a known optical high- z galaxy, which includes spectra, redshifts, line widths, integrated fluxes, CO luminosities, and molecular gas masses. We perform an analysis of the false positive probabilities for each candidate secondary source, characterizing them with a reliability parameter R , and assess the completeness of the search algorithm. We perform a search for optical counterparts corresponding to each candidate source, taking into account the redshift uncertainty for the optical sources in the 3D-HST/CANDELS catalogs. We find that $\sim 64\%$ of these secondary detections have optical counterparts (in some cases more than one) and include these together with an estimate of the probability of association in our catalog. Finally, we use the catalog of candidate sources to build the CO (2 – 1), CO (3 – 2), CO (4 – 3), CO (5 – 4), and CO (6 – 5) luminosity functions for a range of median redshifts, spanning $z \sim 0.6 - 3.6$ and a volume sampled of $\sim 13500 - 57000 \text{ Mpc}^3$ depending on the CO transition. We find broad agreement between our results and those of Walter et al. (2014), Decarli et al. (2016), Riechers et al. (2019), and Decarli et al. (2019). We also demonstrate that a blind CO search across many independent fields in observations of targeted objects can be successfully combined to establish constraints on the luminosity functions of different CO transitions in different redshift bins. We show that, in the case of CO, there appears to be little or no bias towards physically associated neighbors of the primary target down to the luminosities probed. We use an estimate of the cosmic variance to show that an approach which combines multiple independent fields mitigates the impact of cosmic variance. This is because for a contiguous survey area, the volume sampled needs to be very large in order to cut across many different environments; on the order of $10^7 h_{0.7}^{-3} \text{ Mpc}^3$ (for an aspect ratio of 1:1) to decrease cosmic variance to a 10% level according to the formalism by Driver & Robotham (2010). This approach also exploits existing data which can significantly ex-

pand blind survey samples. The caveat is that one must deal with non-uniform sensitivity, which can however be handled through a good SNR characterization of the data sets.

We have derived the molecular gas mass density evolution from converting our high-J CO luminosity functions to CO (1 – 0), assuming a CO luminosity to molecular gas mass conversion factor of $\alpha_{\text{CO}} = 3.6 \text{ M}_{\odot} (\text{K km s}^{-1} \text{ pc}^2)^{-1}$ for consistency with previous studies, and find our results to be largely consistent with previous constraints on the evolution of the cosmic cold gas mass density.

This work made use of PHIBSS ‘The Plateau de Bure HIgh-z Blue Sequence Survey’ (Tacconi et al. 2010). This research has made use of the VizieR catalog access tool, CDS, Strasbourg, France. The original description of the VizieR service was published in (Ochsen-

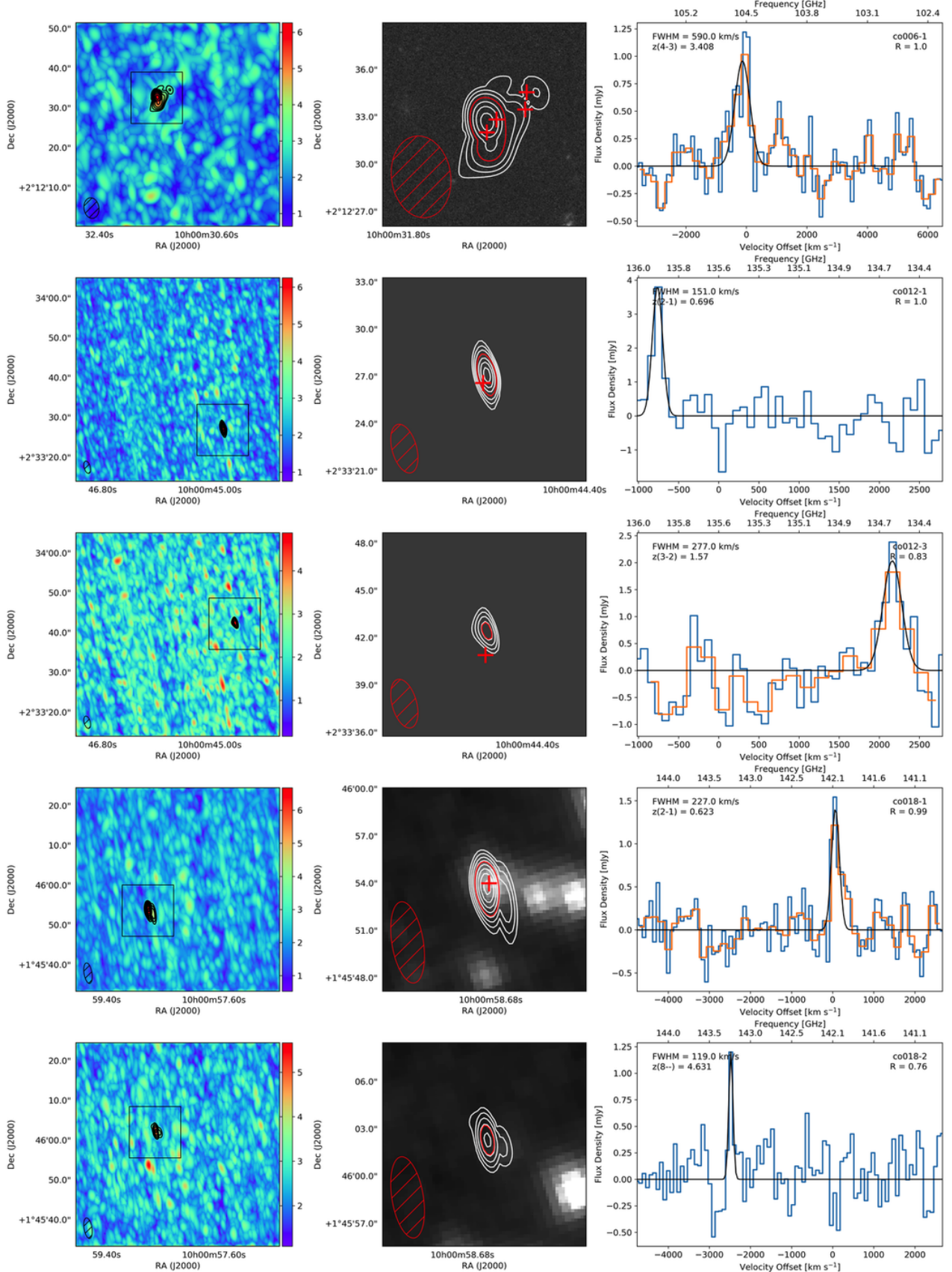
bein et al. 2000). This work is based on observations taken by the 3D-HST Treasury Program (GO 12177 and 12328) with the NASA/ESA HST, which is operated by the Association of Universities for Research in Astronomy, Inc., under NASA contract NAS5-26555. This research has made use of the NASA/IPAC Extragalactic Database (NED) which is operated by the Jet Propulsion Laboratory, California Institute of Technology, under contract with the National Aeronautics and Space Administration. This research made use of APLpy, an open-source plotting package for Python (Robitaille & Bressert 2012). L.L. would like to thank Petr Pokorný for helpful discussions throughout the entirety of this project. L.L. and A.D.B. acknowledge partial support from NSF-AST 1412419. A.D.B. also acknowledges visiting support from the Alexander von Humboldt Foundation.

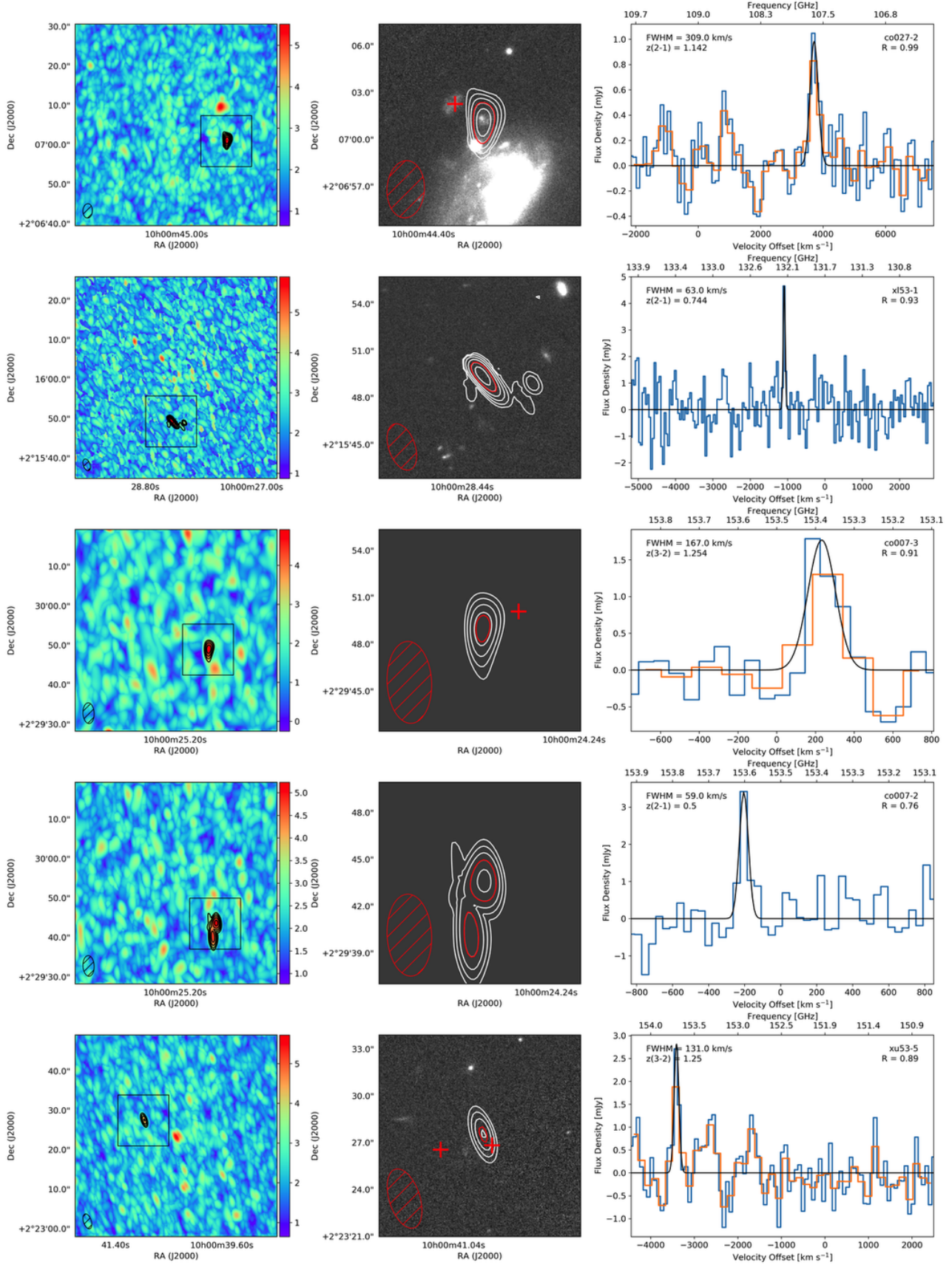
APPENDIX

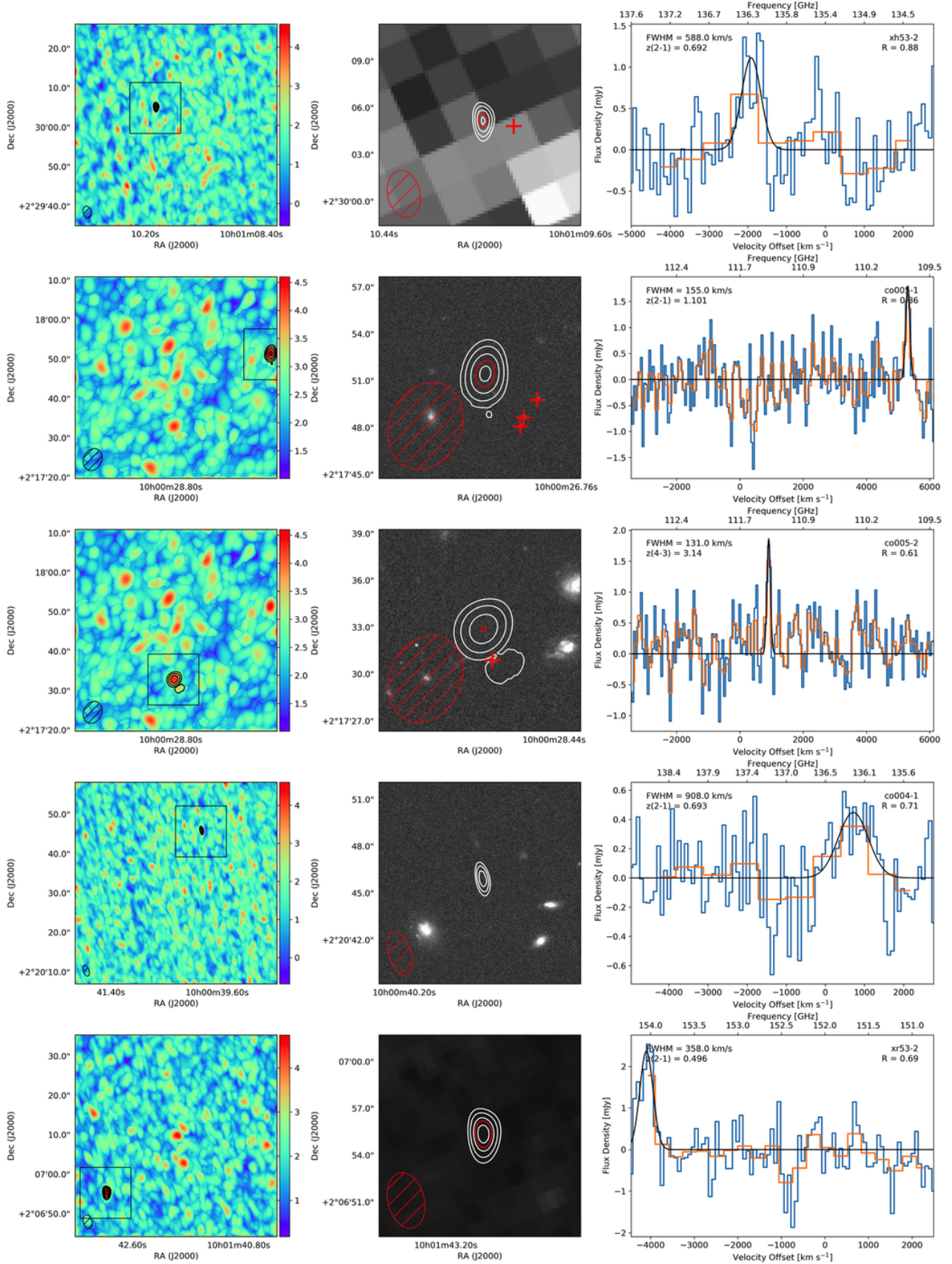
A. DESCRIPTION OF INDIVIDUAL CANDIDATE SOURCES

The following figures show the candidate sources in the COSMOS field, GOODS-N, and EGS/AEGIS. The left panels show the signal-to-noise maps at the velocity resolution where each source is detected with the highest SNR. The black contours start at the 3σ level and increase in steps of 0.5σ . The black box shows the zoom in region for the middle panel images, and the beam is shown in the bottom left corner. The middle panels are HST ACS f814w images where the white contours are the same as in the left panels, the red contour corresponds to the detection threshold (largest negative SNR), red crosses mark the positions of tentative optical counterparts, and the beam is again shown in the bottom left corner. The size of the red contour appears small in some cases, this is however not a problem since these contours are really just the peak of the beam over our adopted “threshold”. The right panel shows the spectrum of each source extracted at the peak pixel, given unresolved sources. The blue spectrum corresponds to a velocity resolution of $\sim 100 \text{ km s}^{-1}$ while the orange spectrum corresponds to the velocity resolution matching that of the left panel. In cases where these two are the same, only the blue lines are shown. The FWHM and redshift of each candidate are added in the top left corners.

Table A lists each candidate source, divided according to the three fields (COSMOS, GOODS-N, EGS/AEGIS) with their RA and Dec, central frequency, flux, FWHM, SNR, and their completeness and reliability measures. Table 3 lists the potential optical counterparts with their IDs, RA and Dec, redshift, and angular separation. Redshifts extracted from the 3D-HST/CANDELS catalogs are photometric redshifts, except where otherwise noted.







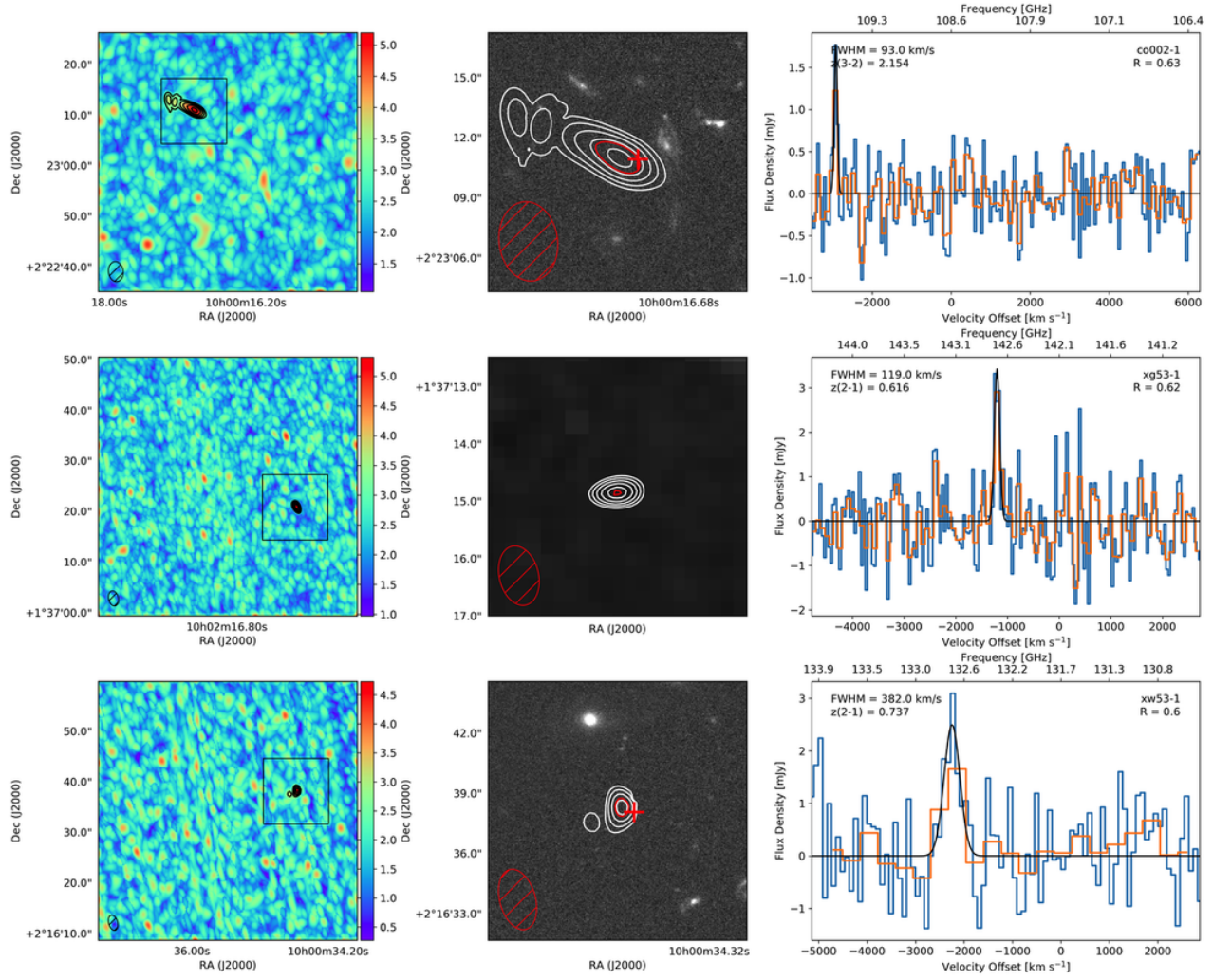
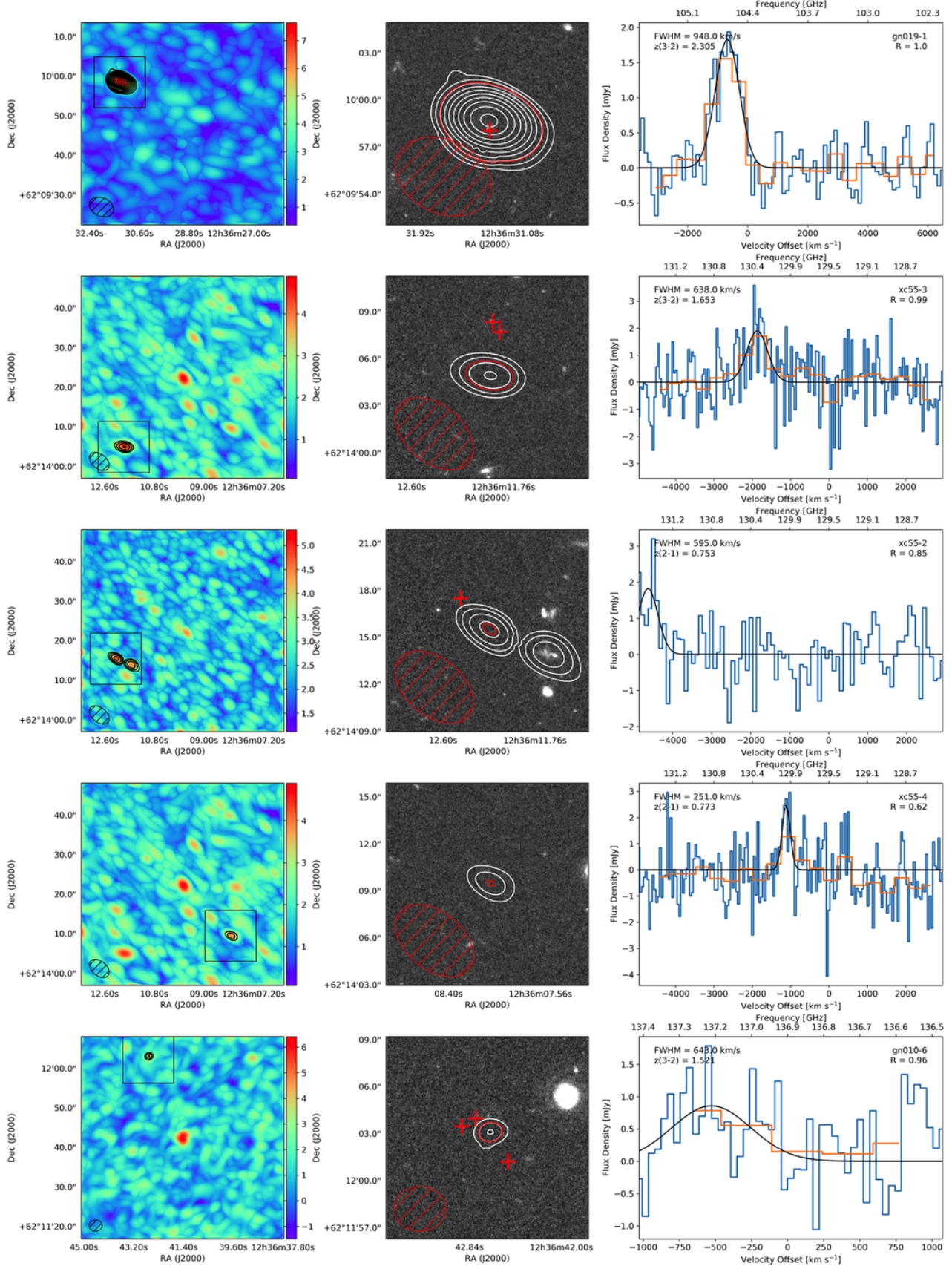


Figure 14. COSMOS



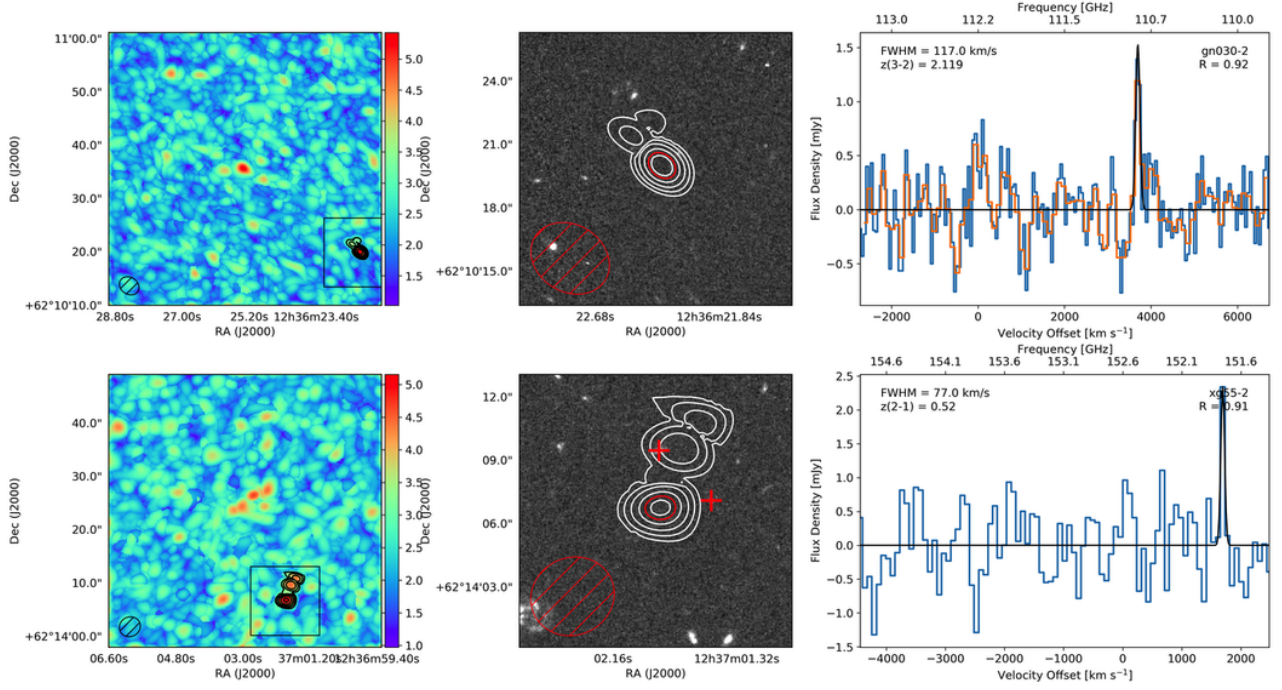
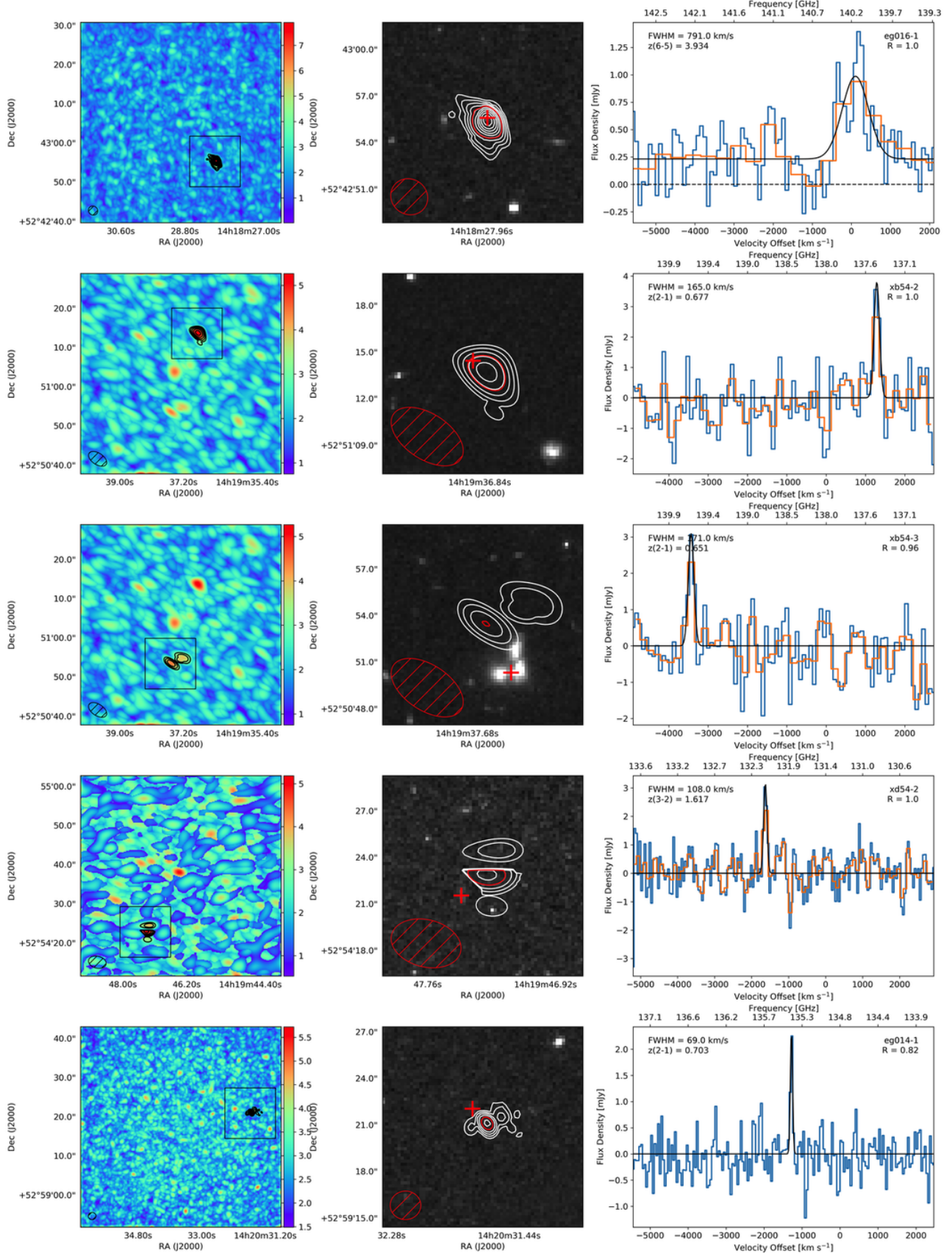


Figure 15. GOODS-N



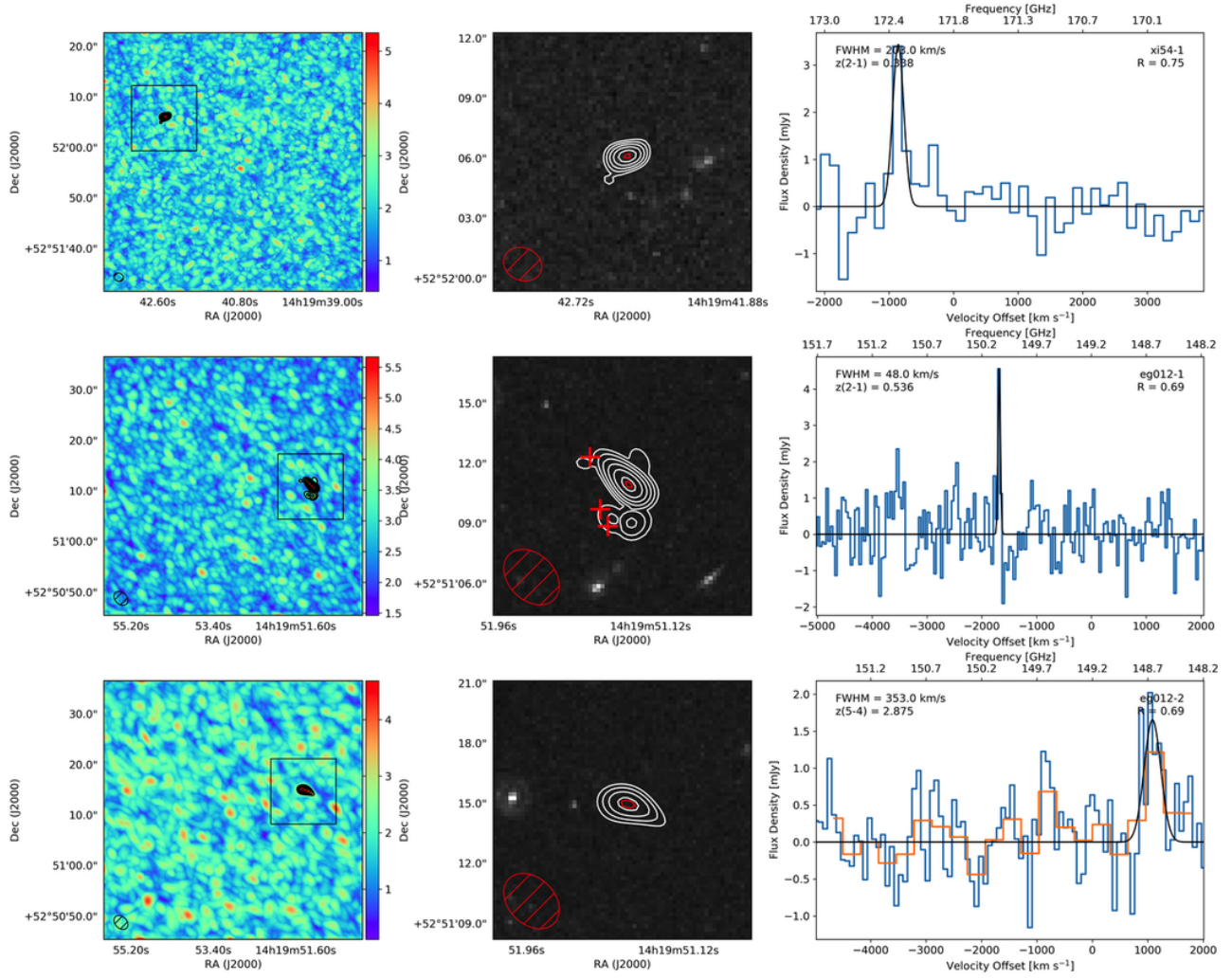


Figure 16. EGS/AEGIS.

Table 2. Properties of Potential detections

ID	RA	Dec	Frequency	Flux	FWHM	SNR	Completeness	Reliability
	(J2000.0)	(J2000.0)	[GHz]	[Jy km s ⁻¹]	[km s ⁻¹]			
COSMOS								
co006-1	10h0m31.44	2d12m32.51s	104.582	0.599 ± 0.139	590 ± 104	6.26	0.9958	1.00
coo06-5	10h0m30.25	2d12m27.91s	102.524	0.172 ± 0.066	141 ± 41	4.48	0.1973	0.35
co012-1	10h0m44.78	2d33m26.80s	135.900	0.613 ± 0.146	151 ± 27	6.25	0.5058	1.00
co012-3	10h0m44.58	2d33m42.20s	134.577	0.599 ± 0.199	277 ± 69	4.88	0.5815	0.83
co018-1	10h0m58.71	1d45m53.60s	142.039	0.341 ± 0.082	227 ± 41	6.68	0.6901	0.99
co018-2	10h0m58.59	1d46m2.000s	143.244	0.152 ± 0.047	119 ± 27	5.15	0.0968	0.76
co027-2	10h0m44.16	2d07m00.93s	107.631	0.323 ± 0.091	309 ± 66	5.50	0.5978	0.99
xl53-1	10h0m28.36	2d15m49.28s	132.169	0.315 ± 0.091	63 ± 14	5.88	0.0061	0.93
xl53-2	10h0m28.99	2d16m9.28s	133.094	0.304 ± 0.107	63 ± 17	5.38	0.0053	0.46
co007-3	10h0m24.64	2d29m48.88s	153.419	0.315 ± 0.100	167 ± 40	4.92	0.2849	0.91
co007-2	10h0m24.52	2d29m43.48s	153.643	0.216 ± 0.053	59 ± 11	5.23	0.1134	0.76
xu53-5	10h0m40.93	2d23m27.44s	153.676	0.392 ± 0.127	131 ± 32	4.54	0.0640	0.89
xu53-6	10h0m40.11	2d23m39.04s	151.627	0.637 ± 0.226	347 ± 93	4.39	0.3436	0.39
xu53-7	10h0m39.35	2d23m03.24s	151.257	0.782 ± 0.298	282 ± 81	4.37	0.6012	0.35
xh53-2	10h1m10.03	2d30m04.90s	136.249	0.696 ± 0.226	588 ± 144	4.58	0.0295	0.88
co005-1	10h0m27.13	2d17m51.20s	109.715	0.297 ± 0.110	155 ± 43	4.60	0.2152	0.86
co005-2	10h0m28.76	2d17m32.80s	111.352	0.260 ± 0.087	131 ± 33	4.34	0.1593	0.61
co005-3	10h0m28.84	2d17m53.20s	109.868	0.166 ± 0.068	91 ± 28	4.33	0.0626	0.59
co004-1	10h0m39.88	2d20m45.64s	136.209	0.432 ± 0.161	908 ± 255	4.37	0.9414	0.71
xr53-2	10h1m43.05	2d06m55.24s	154.097	0.903 ± 0.228	358 ± 68	4.72	0.0095	0.69
xr53-4	10h1m40.33	2d07m07.24s	152.109	1.395 ± 0.366	766 ± 152	4.33	1.0000	0.09
co002-1	10h0m16.88	2d23m10.77s	109.639	0.177 ± 0.053	93 ± 21	5.20	0.0500	0.63
xg53-1	10h2m15.90	1d37m20.80s	142.676	0.435 ± 0.130	119 ± 27	5.32	0.1321	0.62
xw53-1	10h0m34.62	2d16m38.12s	132.701	1.015 ± 0.339	382 ± 97	4.73	0.6225	0.60
xn53-1	10h0m10.05	2d35m46.24s	135.884	0.678 ± 0.221	130 ± 32	5.03	0.1123	0.31
xj53-1	10h1m47.94	2d23m12.00s	114.346	0.461 ± 0.160	69 ± 18	4.81	0.0150	0.08
GOODS-N								
gn019-1	12h36m31.31	62d09m58.47s	104.643	1.840 ± 0.247	948 ± 96	7.64	1.0000	1.00
xc55-3	12h36m11.91	62d14m4.80s	130.324	1.289 ± 0.406	638 ± 152	4.56	0.9729	0.99
xc55-2	12h36m12.19	62d14m15.40s	131.516	1.156 ± 0.530	595 ± 232	4.69	0.9394	0.85
xc55-4	12h36m8.04	62d14m9.40s	129.997	0.660 ± 0.267	251 ± 77	3.85	0.4351	0.62
gn010-6	12h36m42.68	62d12m2.73s	137.174	0.587 ± 0.255	642 ± 215	4.04	0.9459	0.96
gn010-3	12h36m39.05	62d12m2.13s	136.516	0.444 ± 0.184	310 ± 107	4.22	0.7280	0.42
gn030-2	12h36m22.27	62d10m19.82s	110.859	0.190 ± 0.056	117 ± 26	5.32	0.1141	0.92
gn030-3	12h36m26.67	62d10m15.62s	110.809	0.148 ± 0.055	90 ± 26	5.16	0.0420	0.36
xg55-2	12h37m1.87	62d14m06.60s	151.712	0.192 ± 0.105	76 ± 38	5.15	0.0439	0.91
xg55-6	12h37m2.73	62d14m26.60s	151.712	0.277 ± 0.111	156 ± 47	4.13	0.1225	0.13
xa55-2	12h36m59.75	62d15m9.80s	132.414	0.286 ± 0.098	28 ± 8	4.95	0.0156	0.62
gn001-3	12h37m26.27	62d20m39.29s	103.518	0.468 ± 0.191	773 ± 238	4.17	0.5868	0.56

Table 2 continued

Table 2 (*continued*)

ID	RA	Dec	Frequency	Flux	FWHM	SNR	Completeness	Reliability
	(J2000.0)	(J2000.0)	[GHz]	[Jy km s ⁻¹]	[km s ⁻¹]			
xf55-1	12h35m56.17	62d10m46.20s	142.516	0.160 ± 0.173	90 ± 70	4.98	0.0907	0.52
gn011-1	12h37m19.35	62d18m50.56s	137.386	0.543 ± 0.147	136 ± 28	4.85	0.3091	0.51
gn032-1	12h37m16.23	62d15m31.12s	148.202	0.380 ± 0.099	206 ± 41	5.19	0.4593	0.49
gn018-2	12h36m32.26	62d16m03.68s	129.890	0.532 ± 0.225	642 ± 205	4.44	0.5910	0.43
gn018-3	12h36m31.74	62d16m00.48s	128.524	0.595 ± 0.185	637 ± 150	4.35	0.7501	0.27
gn037-2	12h36m25.23	62d10m41.60s	226.683	0.178 ± 0.049	65 ± 14	5.55	0.0113	0.43
gn006-1	12h36m32.72	62d17m48.71s	136.200	0.291 ± 0.091	63 ± 14	5.32	0.0130	0.41
gn007-2	12h36m35.41	62d07m26.53s	145.737	0.431 ± 0.123	154 ± 34	5.29	0.3004	0.41
gn034-2	12h36m20.86	62d19m07.70s	151.152	0.538 ± 0.188	383 ± 101	4.61	0.4066	0.39
gn002-1	12h36m41.56	62d17m01.56s	114.944	0.550 ± 0.158	164 ± 35	4.92	0.2820	0.37
gn021-3	12h36m0.69	62d11m26.18s	142.145	0.303 ± 0.095	58 ± 14	5.40	0.0337	0.37
gn005-1	12h37m18.40	62d12m39.04s	101.340	0.235 ± 0.073	172 ± 42	5.29	0.2278	0.21
gn017-6	12h36m53.43	62d17m04.86s	109.324	0.367 ± 0.132	237 ± 64	4.28	0.3293	0.20
gn017-7	12h36m54.98	62d17m04.26s	106.419	0.320 ± 0.150	191 ± 70	4.27	0.2296	0.18
gn017-1	12h36m53.78	62d17m15.26s	106.817	0.180 ± 0.056	83 ± 19	4.79	0.0490	0.09
gn026-2	12h36m34.68	62d18m02.12s	106.883	0.430 ± 0.168	700 ± 206	4.27	0.7863	0.11
EGS								
eg016-1	14h18m27.95	52d42m55.28s	140.127	0.635 ± 0.158	791 ± 150	7.90	1.0000	1.00
xb54-2	14h19m36.82	52d51m13.60s	137.437	0.669 ± 0.248	165 ± 47	5.27	0.2618	1.00
xb54-3	14h19m37.57	52d50m53.40s	139.610	0.563 ± 0.207	171 ± 47	4.43	0.1678	0.96
xd54-2	14h19m47.37	52d54m22.80s	132.142	0.365 ± 0.112	108 ± 25	5.19	0.0248	1.00
eg014-1	14h20m31.63	52d59m20.86s	135.400	0.175 ± 0.049	69 ± 15	5.72	0.0452	0.82
xi54-1	14h19m42.46	52d52m05.81s	172.316	0.744 ± 0.182	203 ± 37	5.35	0.2646	0.75
eg012-1	14h19m51.28	52d51m10.86s	150.082	0.241 ± 0.080	48 ± 13	5.67	0.0045	0.69
eg012-2	14h19m51.43	52d51m14.66s	148.704	0.622 ± 0.202	353 ± 87	4.69	0.4550	0.69
eg006-3	14h18m44.84	52d43m30.66s	154.766	0.150 ± 0.055	49 ± 14	5.29	0.0277	0.32
eg006-4	14h18m45.72	52d43m37.06s	155.775	0.184 ± 0.099	83 ± 36	5.00	0.0509	0.31
eg006-6	14h18m48.01	52d43m03.46s	154.780	1.262 ± 0.343	829 ± 170	4.46	1.0000	0.25
eg005-1	14h18m58.38	52d42m59.43s	108.805	0.141 ± 0.050	61 ± 18	5.12	0.0163	0.25
eg018-3	14h19m40.06	52d51m38.39s	206.825	0.366 ± 0.122	216 ± 54	4.96	0.2641	0.15

Table 3. Properties of Potential Optical Counterparts

ID	Counterpart ^a	RA ^b	DEC ^b	Redshift ^b	CO Redshift ^c	Δr^d ["]	Association ^e
COSMOS							
co006-1	COS 2997	10h0m31.43	2d12m32.018s	3.5218	3.4084	0.5	0.98
co012-1	COS 33686	10h0m44.79	2d33m26.58s	0.6961 ^f	0.6964	0.2	0.99
co012-3	COS 33774	10h0m44.59	2d33m17.67s	0.6744	1.5695	1.6	0.70
co018-1	COS 485943	10h0m58.69	1d45m54.00s	0.6500	0.6231	0.5	0.98
co027-2	COS 1236431	10h0m44.27	2d7m2.28s	0.9500	1.1419	2.1	0.42
co007-3	COS 2345915	10h0m24.48	2d29m50.10s	1.2500	1.2539	2.7	0.53
xu53-5	COS 20811	10h0m40.88	2d23m26.84s	1.2661	1.2502	1.0	0.89
xu53-6	COS 21168	10h0m40.08	2d23m40.42s	0.6711	0.5204	1.5	0.74
xu53-7	COS 20188	10h0m39.28	2d23m2.68s	1.8406	2.0481	1.2	0.84
xh53-2	COS 2307212	10h1m9.89	2d30m4.82s	0.6700	0.6921	2.2	0.07
co005-1	COS 11546	10h0m26.94	2d17m48.65s	1.1481	1.1012	3.8	0.23
co005-1	COS 11595	10h0m26.88	2d17m49.77s	1.3361	1.1012	4.0	0.15
co005-1	COS 11549	10h0m26.96	2d17m48.09s	0.9379	1.1012	4.0	0.15
co005-2	[Capak2017] 1599172	10h0m28.70	2d17m30.89s	3.116	3.1404	2.1	0.77
co005-3	COS 111603	10h0m29.02	2d17m50.71s	4.2601	4.2451	3.7	0.28
co002-1	COS 20413	10h0m16.82	2d23m10.93s	1.8468	2.1539	1.0	0.89
xw53-1	COS 09632	10h0m34.57	2d16m38.06s	1.6874	1.6058	0.8	0.88
xn53-1	COS 2361883	10h0m9.83	2d35m46.86s	0.7300	0.6966	3.4	0.08
GOODS-N							
gn019-1	GN 05359	12h36m31.29	62d9m58.04s	2.3301 ^g	2.3045	0.5	0.99
xc55-3	GN 18914	12h36m11.79	62d14m7.69s	1.9906	1.6534, 2.5377	3.0	0.52
xc55-3	GN 18951	12h36m11.86	62d14m8.36s	2.0736	0.7690, 1.6534, 2.5377	3.6	0.30
xc55-2	GN 19484	12h36m12.44	62d14m17.49s	3.8340	3.3817, 4.2577	2.7	0.61
gn010-6	GN 11844	12h36m42.78	62d12m3.97s	1.6951	1.5209	1.5	0.64
gn010-6	GN 11803	12h36m42.91	62d12m3.46s	2.2648	1.5209, 2.3610	1.8	0.48
gn010-6	GN 11666	12h36m42.49	62d12m1.21s	1.6462	0.6806, 1.5209, 2.3610	2.0	0.36
xg55-2	GN 18857	12h37m1.50	62d14m7.10s	3.0070	2.7984	2.7	0.20
xg55-2	GN 19030	12h37m1.85	62d14m9.47s	0.4632	0.5196	2.9	0.08
xa55-2	GN 22587	12h36m59.50	62d15m12.37s	0.6726	0.7595	3.1	0.32
gn001-3	GN 36945	12h37m26.17	62d20m39.54s	1.0034	1.2270	0.8	0.96
gn018-2	GN 25624	12h36m32.24	62d16m3.10s	3.1971	3.4366	0.6	0.91
gn018-2	GN 25623	12h36m32.07	62d16m2.86s	0.4247	0.7749	1.5	0.42
gn018-3	GN 25587	12h36m31.77	62d16m1.81s	1.4578	0.7937	1.3	0.57
gn006-1	[BIO2015] GNDV 6325117508	12h36m32.51	62d17m50.80	4.6500	4.9225	1.7	0.59
gn002-1	GN 28898	12h36m41.28	62d17m3.17s	2.3135	2.0084	2.6	0.62
gn002-1	GN 28704	12h36m41.89	62d16m59.95s	1.2792	1.0056, 2.0084	2.8	0.56
gn005-1	GN 13860	12h37m18.08	62d12m39.43s	1.2737	1.2749	2.3	0.69
gn017-6	GN 28920	12h36m53.66	62d17m4.33s	2.2776	2.1630	1.7	0.87
gn017-7	GN 29041	12h36m55.07	62d17m5.93s	2.1137	2.2494	1.8	0.85

Table 3 continued

Table 3 (*continued*)

ID	Counterpart ^a	RA ^b	DEC ^b	Redshift ^b	CO Redshift ^c	Δr^d ["]	Association ^e
gn017-7	GN 28807	12h36m55.02	62d17m1.54s	0.6995	1.1663, 2.2494	2.7	0.67
gn017-1	GN 1308	12h36m54.11	62d17m12.12s	2.5200	2.2373	3.9	0.31
gn026-2	GN 31722	12h36m34.99	62d18m1.07s	1.6652	1.1569, 2.2353	2.4	0.31
EGS							
eg016-1	EGS 33606	14h18m27.92	52d42m55.59s	4.1558	3.9337	0.4	0.95
xb54-2	EGS 16871	14h19m36.89	52d51m14.44s	0.8606	0.6774	1.0	0.93
xb54-3	[Barro2011] 124112	14h19m37.37	52d50m50.32s	0.68	0.6513	3.6	0.15
xd54-2	EGS 21954	14h19m47.52	52d54m21.54s	1.6554	1.6168	1.9	0.69
eg014-1	EGS 10403	14h20m31.70	52d59m22.04s	1.7367	1.5539	1.4	0.11
eg012-1	EGS 06254	14h19m51.40	2d51m9.70s	2.0383	2.0719	1.6	0.55
eg012-1	EGS 06217	14h19m51.36	52d51m8.85s	1.6192	1.3040, 2.0719	2.1	0.22
eg012-1	EGS 06392	14h19m51.46	52d51m12.31s	0.9411	0.5361, 1.3040	2.2	0.15
eg006-3	EGS 23517	14h18m44.64	52d43m32.71s	3.3929	3.4678	2.7	0.16
eg006-4	EGS 23149	14h18m45.56	52d43m37.29s	1.1817	0.4799	1.4	0.78
eg006-6	EGS 18930	14h18m48.11	52d43m3.12s	1.4157 ^g	1.2341, 1.9787	1.8	0.63
eg005-1	EGS 11013	14h18m58.51	52d43m0.15s	1.8040	1.1188, 2.1781	1.4	0.92
eg018-3	EGS 16186	14h19m40.07	52d51m39.71s	1.4787	0.6719, 1.2291, 1.7863	1.3	0.02

^a Designation of the optical counterpart in the COSMOS, GOODS-N, and EGS/AEGIS catalogs.

^b RA, DEC, and redshift (“best”) of the optical counterpart taken from the COSMOS, GOODS-N, and EGS/AEGIS catalogs.

^c List of redshifts corresponding to the possible CO transitions given the posterior likelihood distributions of the EAZY SED fitting.

^d Projected angular separation between candidate source and the potential optical counterpart.

^e For cases where multiple potential optical counterparts exist, we assign a probability of association that is proportional to the inverse square of the projected angular separation.

^f Spectroscopic redshift.

^g Grism redshift.

B. LUMINOSITY FUNCTION CONSTRAINTS: TABULATED RESULTS

In this appendix, we include the 1σ ranges for each luminosity bin, for every CO luminosity function we measure, as shown in Figure 9. Bins are 0.5 dex wide and given in steps of 0.1 dex, therefore every 5th bin is statistically independent; these are shown in bold face.

Table 4. Luminosity functions of the observed CO transitions.

$\log(L'_{\text{CO}})$ bin (K km s ⁻¹ pc ⁻²)	$\log \Phi$, 1 σ (Mpc ⁻³ dex ⁻¹)	$\log(L'_{\text{CO}})$ bin (K km s ⁻¹ pc ⁻²)	$\log \Phi$, 1 σ (Mpc ⁻³ dex ⁻¹)	$\log(L'_{\text{CO}})$ bin (K km s ⁻¹ pc ⁻²)	$\log \Phi$, 1 σ (Mpc ⁻³ dex ⁻¹)
CO(2-1), $z \sim 0.34 - 0.79$		CO(2-1), $z \sim 1.01 - 1.27$		CO(3-2), $z \sim 1.22 - 1.66$	
8.4–8.9	-3.79 , -2.93	9.0–9.5	-3.16 , -1.80	9.0–9.5	-2.91 , -2.25
8.5–9.0	-3.17 , -2.51	9.1–9.6	-3.16 , -1.80	9.1–9.6	-2.86 , -2.31
8.6–9.1	-3.17 , -2.51	9.2–9.7	-3.19 , -2.34	9.2–9.7	-2.86 , -2.31
8.7–9.2	-3.17 , -2.51	9.3–9.8	-3.20 , -2.72	9.3–9.8	-2.85 , -2.37
8.8–9.3	-3.11 , -2.46	9.4–9.9	-3.71 , -3.28	9.4–9.9	-3.39 , -2.84
8.9–9.4	-3.10 , -2.54	9.5–10.0	-3.67 , -3.27	9.5–10.0	-3.43 , -2.88
9.0–9.5	-3.49 , -2.83	9.6–10.1	-3.67 , -3.27	9.6–10.1	-3.85 , -3.37
9.1–9.6	-3.28 , -2.85	9.7–10.2	-3.75 , -3.32	9.7–10.2	-3.85 , -3.37
9.2–9.7	-3.04 , -2.74	9.8–10.3	-4.13 , -3.47	9.8–10.3	-4.37 , -3.82
9.3–9.8	-3.09 , -2.77	9.9–10.4	-4.37 , -3.02	9.9–10.4	-4.42 , -3.87
9.4–9.9	-3.16 , -2.80	–	–	10.0–10.5	-5.04 , -4.38
9.5–10.0	-3.16 , -2.80	–	–	10.1–10.6	-5.10 , -3.74
9.6–10.1	-3.31 , -2.88	–	–	10.2–10.7	-5.10 , -3.74
9.7–10.2	-5.37 , -4.02	–	–	10.3–10.8	-5.10 , -3.74
9.8–10.3	-5.37 , -4.02	–	–	–	–
9.9–10.4	-5.37 , -4.02	–	–	–	–
10.0–10.5	-5.37 , -4.02	–	–	–	–
CO(3-2), $z \sim 2.01 - 2.31$		CO(4-3), $z \sim 1.03 - 1.98$		CO(4-3), $z \sim 2.05 - 2.59$	
9.1–9.6	-3.37,-2.01	8.8–9.3	-7.88,-6.53	9.1–9.6	-2.5,-1.14
9.2–9.7	-3.34,-2.68	8.9–9.4	-7.88,-6.53	9.2–9.7	-2.5,-1.14
9.3–9.8	-3.34,-2.68	9.0–9.5	-7.88,-6.53	9.3–9.8	-2.5,-1.14
9.4–9.9	-3.34,-2.68	9.1–9.6	-7.88,-6.53	9.4–9.9	-2.5,-1.14
9.5–10.0	-3.36,-2.87	9.2–9.7	-4.91,-4.06	9.5–10.0	-2.57,-1.72
9.6–10.1	-3.81,-3.38	9.3–9.8	-4.83,-3.47	9.6–10.1	-4.69,-3.84
9.7–10.2	-4.41,-3.86	9.4–9.9	-4.83,-3.47	9.7–10.2	-4.69,-3.84
9.8–10.3	-4.32,-3.84	9.5–10.0	-4.83,-3.47	9.8–10.3	-4.69,-3.84
9.9–10.4	-4.32,-3.84	9.6–10.1	-4.83,-3.47	9.9–10.4	-4.64,-3.98
10.0–10.5	-4.66,-4.0	9.7–10.2	-5.43,-4.07	10.0–10.5	-4.97,-4.12
10.1–10.6	-4.8,-3.44	9.8–10.3	-5.43,-4.07	10.1–10.6	-5.22,-3.87
10.2–10.7	-4.8,-3.44	9.9–10.4	-5.43,-4.07	10.2–10.7	-5.22,-3.87
10.3–10.8	-4.28,-2.93	10.0–10.5	-5.43,-4.07	10.3–10.8	-5.22,-3.87
10.4–10.9	-4.28,-2.93	10.1–10.6	-5.43,-4.07	–	–
10.5–11.0	-4.28,-2.93	–	–	–	–
10.6–11.1	-4.28,-2.93	–	–	–	–
10.7–11.2	-4.28,-2.93	–	–	–	–
CO(4-3), $z \sim 3.14 - 3.40$		CO(5-4), $z \sim 3.38 - 3.44$		CO(5-4), $z \sim 4.25 - 4.51$	

Table 4 continued

Table 4 (*continued*)

$\log(L'_{\text{CO}})$ bin (K km s ⁻¹ pc ⁻²)	$\log \Phi$, 1σ (Mpc ⁻³ dex ⁻¹)	$\log(L'_{\text{CO}})$ bin (K km s ⁻¹ pc ⁻²)	$\log \Phi$, 1σ (Mpc ⁻³ dex ⁻¹)	$\log(L'_{\text{CO}})$ bin (K km s ⁻¹ pc ⁻²)	$\log \Phi$, 1σ (Mpc ⁻³ dex ⁻¹)
9.4–9.9	-3.96,-2.6	9.5–10.5	-5.66,-4.81	9.2–10.2	-4.66,-3.8
9.5–10.0	-3.96,-2.6	–	–	–	–
9.6–10.1	-3.96,-2.6	–	–	–	–
9.7–10.2	-3.96,-2.6	–	–	–	–
9.8–10.3	-3.96,-3.1	–	–	–	–
9.9–10.4	-4.66,-3.3	–	–	–	–
10.0–10.5	-4.66,-3.3	–	–	–	–
10.1–10.6	-4.66,-3.3	–	–	–	–
10.2–10.7	-4.66,-3.3	–	–	–	–
CO(6-5), $z \sim 3.47 - 3.93$					
8.8–9.8	-5.05,-4.2				

REFERENCES

- Blain, A. W., Smail, I., Ivison, R. J., Kneib, J. P., & Frayer, D. T. 2002, *PhR*, 369, 111
- Bolatto, A. D., Wolfire, M., & Leroy, A. K. 2013, *ARA&A*, 51, 207
- Bolatto, A. D., Warren, S. R., Leroy, A. K., et al. 2015, *ApJ*, 809, 175
- Brammer, G. B., van Dokkum, P. G., & Coppi, P. 2008, *ApJ*, 686, 1503
- Brammer, G. B., van Dokkum, P. G., Franx, M., et al. 2012, *ApJS*, 200, 13
- Carilli, C. L., & Walter, F. 2013, *ARA&A*, 51, 105
- Carleton, T., Cooper, M. C., Bolatto, A. D., et al. 2017, *MNRAS*, 467, 4886
- Casey, C. M., Narayanan, D., & Cooray, A. 2014, *PhR*, 541, 45
- Daddi, E., Bournaud, F., Walter, F., et al. 2010, *ApJ*, 713, 686
- Daddi, E., Dannerbauer, H., Liu, D., et al. 2015, *A&A*, 577, A46
- Decarli, R., Walter, F., Carilli, C., et al. 2014, *ApJ*, 782, 78
- Decarli, R., Walter, F., Aravena, M., et al. 2016, *ApJ*, 833, 69
- Decarli, R., Carilli, C., Casey, C., et al. 2018, in *Astronomical Society of the Pacific Conference Series*, Vol. 517, *Science with a Next Generation Very Large Array*, ed. E. Murphy, 565
- Decarli, R., Walter, F., González-López, J., et al. 2019, *arXiv e-prints*, arXiv:1903.09164
- Driver, S. P., & Robotham, A. S. G. 2010, *MNRAS*, 407, 2131
- Freundlich, J., Combes, F., Tacconi, L. J., et al. 2019, *A&A*, 622, A105
- Gehrels, N. 1986, *ApJ*, 303, 336
- Genzel, R., Tacconi, L. J., Gracia-Carpio, J., et al. 2010, *MNRAS*, 407, 2091
- Genzel, R., Tacconi, L. J., Lutz, D., et al. 2015, *ApJ*, 800, 20
- González-López, J., Decarli, R., Pavesi, R., et al. 2019, *arXiv e-prints*, arXiv:1903.09161
- Greve, T. R., Bertoldi, F., Smail, I., et al. 2005, *MNRAS*, 359, 1165
- Guilloteau, S., Delannoy, J., Downes, D., et al. 1992, *A&A*, 262, 624
- Kent, S. M., & Gunn, J. E. 1982, *AJ*, 87, 945
- Komatsu, E., Smith, K. M., Dunkley, J., et al. 2011, *ApJS*, 192, 18
- Lagos, C. D. P., Baugh, C. M., Lacey, C. G., et al. 2011, *MNRAS*, 418, 1649
- Lagos, C. d. P., Bayet, E., Baugh, C. M., et al. 2012, *MNRAS*, 426, 2142
- Madau, P., & Dickinson, M. 2014, *ARA&A*, 52, 415
- Momcheva, I. G., Brammer, G. B., van Dokkum, P. G., et al. 2016, *ApJS*, 225, 27
- Obreschkow, D., Heywood, I., Klöckner, H.-R., & Rawlings, S. 2009, *ApJ*, 702, 1321
- Ochsenbein, F., Bauer, P., & Marcout, J. 2000, *A&AS*, 143, 23
- Pavesi, R., Sharon, C. E., Riechers, D. A., et al. 2018, *ApJ*, 864, 49
- Popping, G., Pérez-Beaupuits, J. P., Spaans, M., Trager, S. C., & Somerville, R. S. 2014a, *MNRAS*, 444, 1301
- . 2014b, *MNRAS*, 444, 1301
- Popping, G., van Kampen, E., Decarli, R., et al. 2016, *MNRAS*, 461, 93
- Popping, G., Pillepich, A., Somerville, R. S., et al. 2019, *arXiv e-prints*, arXiv:1903.09158
- Riechers, D. A., Pavesi, R., Sharon, C. E., et al. 2019, *ApJ*, 872, 7
- Robitaille, T., & Bressert, E. 2012, *APLpy: Astronomical Plotting Library in Python*, *Astrophysics Source Code Library*, , ascl:1208.017
- Rubin, V. C., Burstein, D., Ford, Jr., W. K., & Thonnard, N. 1985, *ApJ*, 289, 81
- Schechter, P. 1976, *ApJ*, 203, 297
- Schuster, K.-F. 2014, https://www.iram-institute.org/medias/uploads/IRAM_2014.pdf
- Skelton, R. E., Whitaker, K. E., Momcheva, I. G., et al. 2014, *ApJS*, 214, 24
- Solomon, P. M., Downes, D., Radford, S. J. E., & Barrett, J. W. 1997, *ApJ*, 478, 144
- Tacconi, L. J., Genzel, R., Neri, R., et al. 2010, *Nature*, 463, 781
- Tacconi, L. J., Neri, R., Genzel, R., et al. 2013, *ApJ*, 768, 74
- Tacconi, L. J., Genzel, R., Saintonge, A., et al. 2018, *ApJ*, 853, 179
- Vallini, L., Gruppioni, C., Pozzi, F., Vignali, C., & Zamorani, G. 2016, *MNRAS*, 456, L40
- Walter, F., Decarli, R., Sargent, M., et al. 2014, *ApJ*, 782, 79
- Walter, F., Decarli, R., Aravena, M., et al. 2016, *ApJ*, 833, 67
- Whitaker, K. E., Pope, A., Cybulski, R., et al. 2017, *ApJ*, 850, 208
- Wuyts, S., Förster Schreiber, N. M., Lutz, D., et al. 2011, *ApJ*, 738, 106